POLITECNICO DI TORINO

Master degree course in Electronic Engineering

Master Degree Thesis

Analysis of Semiconductor Silicon-Based Heterostructure Quantum Dots for Qubit Systems

Supervisors
Prof.ssa Mariagrazia Graziano
Prof. Gianluca Piccinini
Dott. Antonio Tudisco

Candidate
Giovanni Pedicini

July 2024

To my beloved parents, Alessia and Sandro,
and to the memory of my dearest grandparents,
Teresa, Carmela, Rolando, Giovanni

Contents

Part I

General Introduction

Chapter 1

This chapter aims to give an introduction to semiconductor quantum computing by highlighting its advantages. The semiconductor's ability to dimensionally confine the particle using voltage and heterostructure is then analyzed. Finally, it describes the transport analysis theory used in semiconductor quantum computing. For more information, you can consult [1].

1.1 Semiconductor Quantum Computing

1.1.1 Semiconductor Properties

Semiconductors are crystalline structures wherein atoms are arranged periodically, possessing properties that lie between conductors and insulators in terms of electrical conductivity. The crucial electronic properties of semiconductors stem from their crystalline structure. Specifically, their intermediate behavior arises from the specific electronic structure they possess, which consists of two bands:

- The **Conduction Band** is the energy band where electrons are free to move under the influence of an electric field. There, electrons have higher energy and are not bound to any specific atom.
- **The Valence Band** is the energy band where electrons are tightly bound to atoms and cannot move freely. Electrons, in this case, have lower energy compared to those in the conduction band.

These two bands are separated by a characteristic energy gap known as the **band gap**. The relationship between the energy and momentum of electrons can be explained using reciprocal space, where each point represents a set of potential wavevectors (k-vectors) corresponding to plane waves that satisfy the periodicity of the crystal lattice. Specifically, this periodicity is defined by the Brillouin First Zone (Fig.1.1), which is the smallest region in reciprocal space containing all possible wave vectors for electrons that can propagate through the crystal lattice without being influenced by the lattice periodicity.

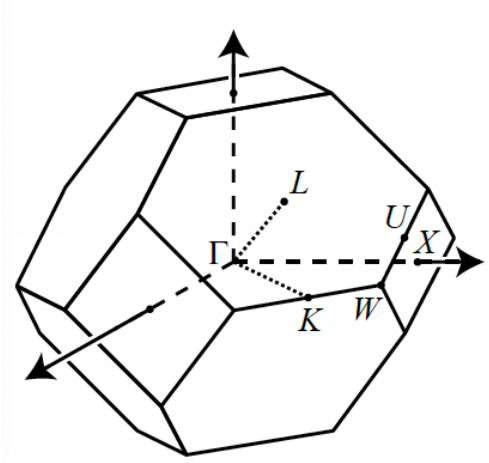

Figure 1.1. First Brillouin zone of the fcc lattice. The points Γ , X, L, and others are indicated. Specifically, Γ is the First Brillouin zone center, X is the center of the square face, and L is the center of the hexagonal face. Adapted from [1].

Γ	(0,0,0)
X	(1,0,0)
L	(1/2,-1/2,1/2)
U	(1,-1/4,1/4)
K	(-3/4,3/4,0)
W	(1,$\sqrt{2}$/2,0)

Figure 1.2. Coordinates of symmetry points in the reciprocal lattice of a face–centered cubic (fcc) lattice type, where each lattice point is surrounded by eight nearest neighbors located at the corners of a cube. Additionally, there are six more neighbors positioned at the center of each face of the cube. Lengths are in units of $2\pi/a$, where a is the lattice constant. Adapted from [1].

When analyzing the band model in reciprocal space, the energy-momentum relation of electrons is described by the dispersion relation [2].

$$E(\underline{k}) = Ec + \frac{\hbar^2 |\underline{k}|^2}{2m}, \tag{1.1}$$

where

$$\underline{k}^2 = {k_x}^2 + {k_y}^2 + {k_z}^2 \tag{1.2}$$

$\underline{k}$ is the wavevector of the electron with its component k_x, k_y and k_z, E is its energy, m is the electron mass and Ec is the minimum of the conduction band. In particular, the wave vector is obtained through the De Broglie relationship [1]:

$$\underline{p} = \hbar \underline{k} \tag{1.3}$$

where p is the momentum, k is the wavevector and $\hbar$ is the Plank constant divided by 2π. The *De Broglie relationship* aids the understanding of how electrons flow inside crystal lattices, how their energy changes about momentum, and how they react to external forces or electric fields in semiconductors. Specifically, remembering that the *De Broglie wavelength* is $\lambda = \frac{2\pi}{k}$, it provides insight into how electron wavefunctions interact with the periodic potential of the lattice, affecting their behavior, such as scattering and interference effects. When considering the alteration of their energy concerning momentum, changes in the latter correspond to equivalent changes in the *De Broglie wavelength*. This relationship aids in comprehending how electron energy varies as it traverses the semiconductor lattice or interacts with other particles. Lastly, in semiconductors, the *De Broglie wavelength relationship* clarifies how electrons react to outside forces or electric fields. For instance, electrons accelerate when exposed to an electric field, which modifies their momentum and, consequently, the *De Broglie wavelength* that corresponds with it.

1.1.2 Technology Advantage

The previous decade witnessed a continuous advancement in quantum devices constructed from semiconductor materials. Indeed, this trend arose from the significant limitations encountered by classical electronics across numerous applications. Quantum electronics, especially quantum computing, emerged as a promising solution for achieving functionalities that are not possible with classical electronics. Various technologies have been proposed to foster the development of quantum technologies, with Semiconductor Quantum Technologies being among the most promising.

Semiconductor devices provide the capability to construct qubits with extended decoherence time, which refers to the duration during which the qubit retains accurate information [3]. As a result, obtaining very high fidelity, which describes the level of agreement between the actual output of an operation and the planned state [4], in gate implementation through semiconductor qubits is now conceivable. Solid-state quantum computing devices based on semiconductors can be developed by leveraging existing technologies used in classical devices. Consequently, semiconductor technology presents a compelling opportunity for scalable and miniaturized solid-state quantum computing.

After decades of advancement, it became evident that silicon was the optimal material for next-generation devices leveraging quantum properties of charge and spin. Recently, significant progress has been made in the treatment and analysis

of quantum phenomena in silicon. Furthermore, in silicon technology, it is possible to describe single electron confinement physics and observe spin blockade, which was previously unattainable in other semiconductor materials [5]. Specifically, spin blockade consists of a phenomenon in which the transport of electrons through a quantum dot is blocked due to the Pauli exclusion principle, and it occurs only when the energy levels of the quantum dot are aligned such that only electrons with specific spin orientations can occupy them [6].

1.1.3 Silicon

The two devices analyzed in this thesis are also based on silicon since it is among the most commonly used semiconductors in electronics. Silicon possesses a crystalline structure known as a diamond cubic structure, which belongs to the fcc lattice type mentioned earlier. In this structure, each silicon atom forms covalent bonds with four neighboring silicon atoms, resulting in a tetrahedral arrangement. This arrangement creates a robust three-dimensional network of covalent bonds throughout the crystal lattice.

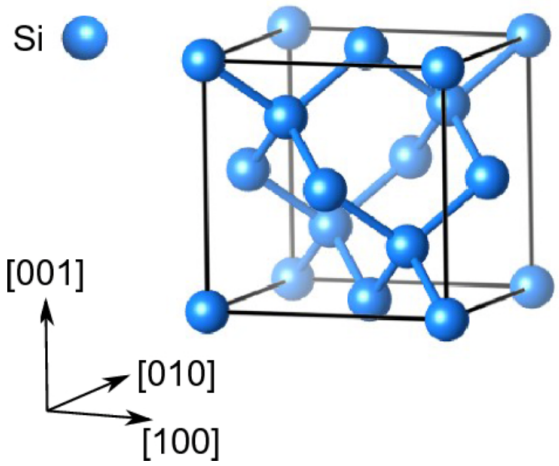

Figure 1.3. Silicon Crystal structure with the diamond lattice, the three axes indicate the different orientation.Adapted from [7].

When analyzing the energy-momentum relation of electrons in silicon, it becomes apparent that it has an indirect band gap of approximately 1.1 eV at room temperature. An indirect band gap implies that the minimum of the conduction band has a different wavevector (and, as a consequence, a different momentum) compared to the maximum of the valence band, and the silicon features six degenerate minima in the conduction band [1].

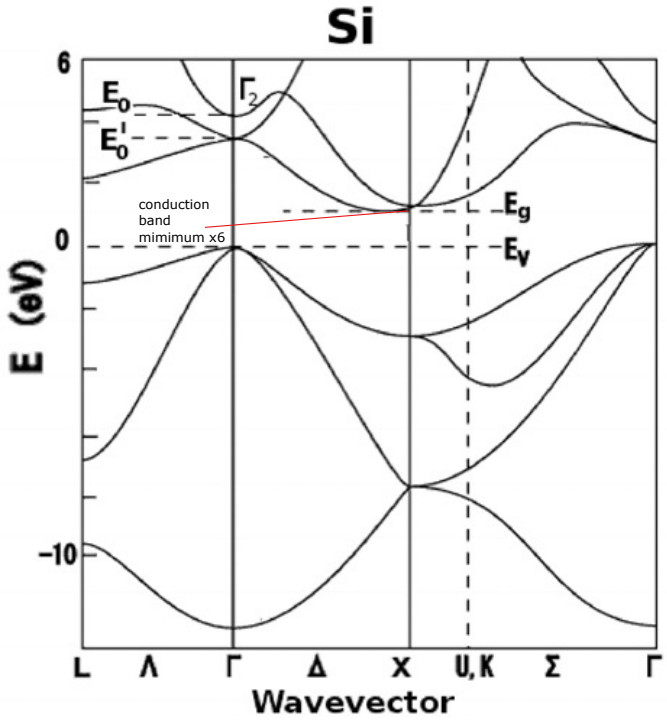

Figure 1.4. The energy-momentum relation of silicon is examined, with a focus on the six minima in the conduction band. Adapted from [8].

1.2 Quantum Confinement Semiconductors

One crucial aspect of quantum computing involves the capability to generate quantum confinement particles through specific heterostructures or precise application of electric potential. Specifically, quantum confinement refers to the phenomena where electron or other particle motion is restricted in a very small region. The objective of this section is thus to elucidate the theory of quantum confinement particles for both scenarios [9]. Moreover, this analysis serves as the foundation for comprehending the more intricate phenomena governing quantum mechanics theory in quantum computing.

1.2.1 Quantum Confinement Heterostructures

A quantum confinement heterostructure denotes a semiconductor device or material structure designed to exploit quantum confinement effects, thereby controlling the behavior of electrons and other charge carriers at the nanoscale. Quantum confinement arises when the dimensions of a material approach the *De Broglie wavelength* of the particles, such as electrons, within that material. [1]. The term "heterostructure" signifies that the material comprises various semiconductor materials with differing band gaps. This is done to establish potential energy barriers and wells, enabling precise regulation of the movement and confinement of charge carriers.

However, it is important to acknowledge that the materials composing the heterostructure may possess different lattice constants, representing the distance between two adjacent atoms. Despite employing precise epitaxial growth techniques, there remains a possibility that lattice mismatches between materials could induce stress and, consequently, defects in the structure.

Confinement along the growth direction is achieved through the difference between material band gaps, creating a discontinuity within the conduction and valence bands. By engineering the structure in a specific manner, it becomes feasible to confine carriers (electrons and holes) within a particular layer, quantizing the carriers along the growth direction.

In the field of semiconductor heterostructures like quantum wells, wires, or dots, quantum confinement arises when the size of the structure becomes comparable to or smaller than the wavelength of electrons, rendering quantum effects relevant. Consequently, the analysis of the system necessitates the application of quantum mechanics and cannot be conducted using classical methods. In classical analysis, it is assumed that particles in a confined structure can possess any energy or remain stationary at zero energy, termed the ground state. Conversely, when analyzing the system through quantum mechanics, this confinement results in the quantization of energy levels. This implies that only specific discrete energy levels are allowed for the confined structure particle and the ground state always possesses energy different from zero.

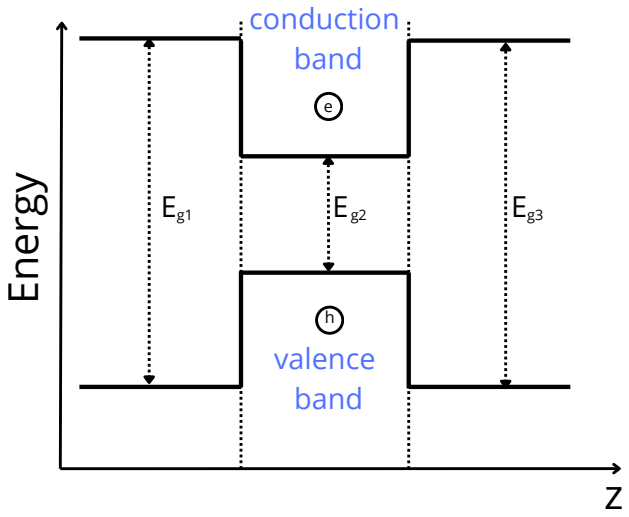

Figure 1.5. A band diagram of a heterostructure is depicted, showcasing the engineering of different band gaps to confine electrons and holes within the middle layer.

Specifically, when considering only one-dimensional confinement along the z-direction and assuming infinite confinement barriers, the energy levels of a particle are determined by:

$$E_z(n_z) = \frac{n_z^2 \pi^2 \hbar^2}{2mL_z^2}, \tag{1.4}$$

where m is the mass particle, L_z is the width of the structure along z direction n_z is an integer number called quantum number which is associated with the energy level ($n_z = 1$ is the ground state, when n_z is equal to the largest possible value corresponds to the highest level). However, the formula for E_z yields more bound states than the actual value, as it assumes an infinite barrier potential. The confinement will modify the energy-momentum relation because the subbands are created as described in the following formula:

$$E(n_z) = E_c + E_z(n_z) + \frac{\hbar^2(k_x^2 + k_y^2)}{2m}, \tag{1.5}$$

where E_c is the minimum of the conduction band, $k_x = \sqrt{\frac{2m}{\hbar^2}E_x}$ and $k_y = \sqrt{\frac{2m}{\hbar^2}E_y}$ are wavevector component along the y and x axes, with E_x and E_y are the kinetic particle energy in such direction. This implies that the energy levels of the electrons become quantized, leading to the formation of n_z discrete energy levels known as subbands, each having 2D dispersion relation $E(k_x, k_y)$ as described in [9].

In conclusion, the quantum effect will also affect the Density of States (DOS), which represents the distribution of available states for particles as a function of energy. The formula for the bulk DOS is:

$$N(E) = \frac{1}{2\pi^2}\left(\frac{2m}{\hbar^2}\right)^{3/2}\sqrt{E} \tag{1.6}$$

Specifically, the square-root behavior of energy predicted by classical laws is no longer applicable due to quantum effects. This change leads to the density of states losing its energy dependence and adopting different formulas depending on the number of quantized directions.

Here is a brief overview of various quantum confinement structures:

Quantum Wells	Thin layers of semiconductor material sandwiched between two layers of a different semiconductor. Electrons are confined to move in two dimensions within these structures.
Quantum Wires	These are narrow regions where electrons are confined to move in one dimension.
Quantum Dots	These are small semiconductor particles with sizes typically on the order of nanometers. Electrons are confined in all three dimensions, resulting in discrete energy levels.

Figure 1.6. Brief overview of various quantum confinement structures

1.2.2 Quantum Dots

In this thesis, the emphasis is placed on quantum dots where confinement occurs in all three dimensions. Hence, there are no dispersion curves, as the vectorial component of E does not depend on any k-vector component. Indeed, the dispersion relation in a quantum dot, assuming equal lengths in all three dimensions ($L_x = L_y = L_z = L$), is:

$$E_{n_z,n_y,n_x} = E_c + E_z(n_z) + E_y(n_y) + E_x(n_x) = E_c + \frac{\pi^2\hbar^2}{2mL^2}(n_x^2 + n_y^2 + n_z^2) \tag{1.7}$$

From the moment that the energies depend only on n_x, n_y, and n_z (that are quantum numbers) consequently, the DOS results in a series of $\delta - function$ centered at the energy level.

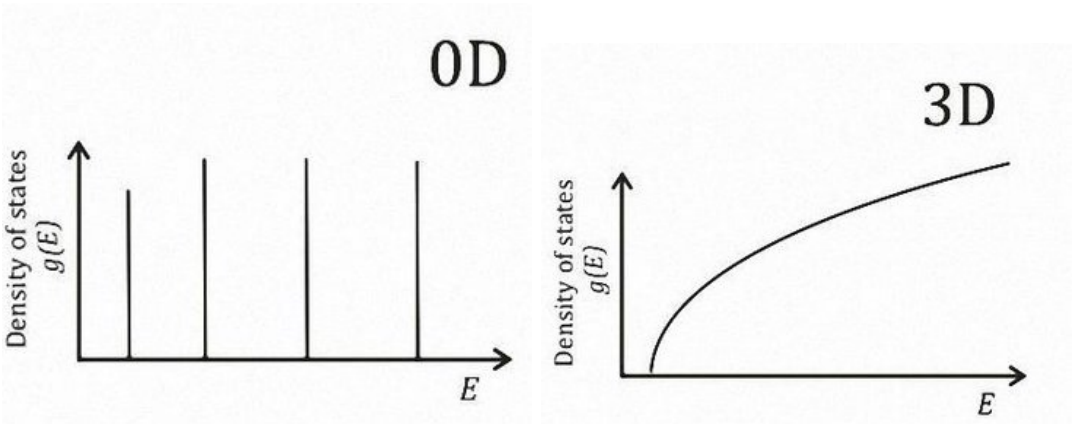

(a) DOS 0D (b) DOS 3D

Figure 1.7. Figure 1.7(a) represents the density of states in the Quantum Dot when the motion of the particle is limited in all three directions. Figure 1.7(b) represents the density of states in the Bulk materials, where the electrons are free to move in all directions. Adapted from [10].

1.3 Coulomb Peaks and Coulomb Diamonds

The definition of the chemical potential of the dot for a particular energy level involves the energy difference between the dot's states with different occupancies: $\mu_{dot}(N+1) = E(N+1) - E(N)$, where $E(N)$ denotes the total energy of the dot when occupied by N electrons. In this setup, electrons tunnel from the source to the dot, resulting in a transition from N to N+1 electrons in the dot, followed by subsequent tunneling toward the drain. This process induces fluctuations in the electron count within the dot, leading to observable peaks in conductance, known as **Coulomb peaks**. These peaks are observed at specific gate voltages that facilitate the incremental filling of the dot with individual electrons [11]. However, it is mandatory to acknowledge that the ideal scenario, where a voltage variation of 1 V corresponds precisely to an energy shift of 1 eV, is typically unattainable in real systems. This discrepancy necessitates consideration of the lever arm, an adimensional coefficient that characterizes a gate's actual effectiveness in tuning the chemical potential of the dot. The observation of Coulomb peaks entails a meticulous process: measuring electron flow across a quantum dot by applying a narrow source-drain bias window (the difference between the chemical potential of the source (μ_s) and the drain (μ_d)), while finely adjusting the gate voltage. These peaks become apparent at specific gate voltages when the electrochemical potential of the quantum dot (μ_{dot}) falls within the source-drain bias window.

$$\mu = \mu_0 - e\alpha V_g \tag{1.8}$$

where α is the lever arm of that specific gate.

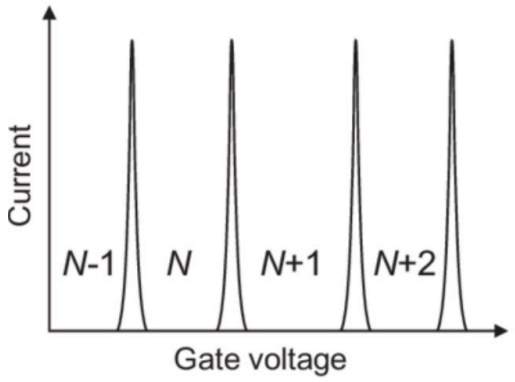

Figure 1.8. Coulomb peaks in current versus the gate voltage. Adapted from [12].

A similar analysis is performed to obtain the coulomb diamonds. They describe the behavior of the differential conductance versus the source-drain voltage and the gate voltage. For this reason, the two voltages are tuned and, for each configuration, the differential conductance is computed. In particular, the gate voltage is considered on the x-axis while the source-drain voltage is on the y-axis. The obtained result is a series of diamonds representing the blockade regions, that correspond to specific configurations of gate and source-drain voltage. Especially, these configurations determine a quantized occupation number of electrons due to Coulomb repulsion.
Finally, the plot (Fig 1.9), along the x-axis, starts with the diamond representing the configuration with zero electrons, followed by a series of diamonds representing successive quantized occupation numbers of electrons [13, 14].

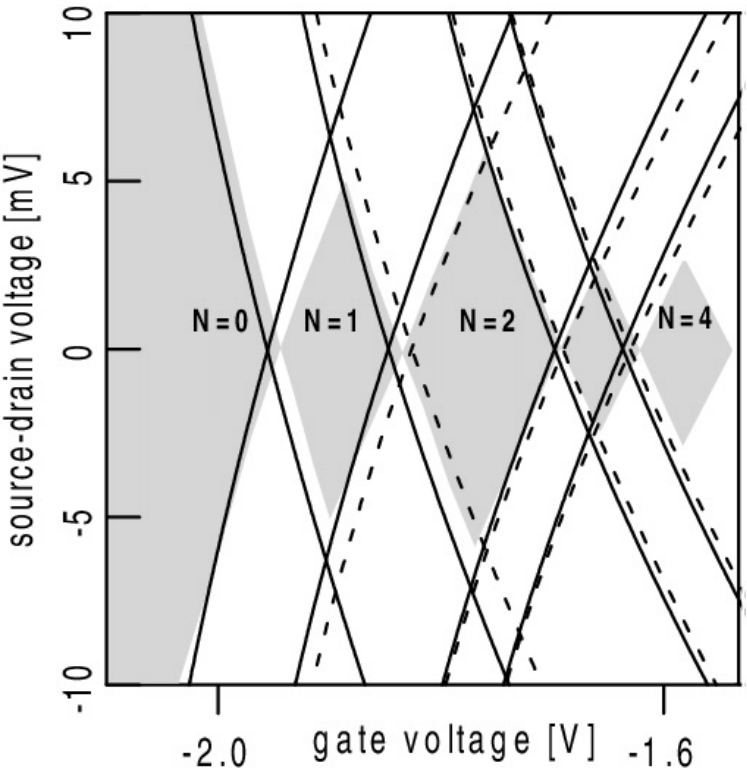

Figure 1.9. Coulomb Diamonds representation. The differential conductance is nearly zero in the grey region, while the dashed and solid lines represent the boundaries of transport windows. Lastly, the number of electrons is fixed in each Coulomb blockade region. Adapted from [15].

1.4 Charge Stability Diagram

An in-depth examination involves analyzing the occupancy dynamics of quantum dots as the voltages applied to the plunger gates vary. This analysis is typically visualized through a charge stability diagram, a fundamental representation in quantum dot research. Considering a double quantum dot system, Figure 1.10(a) depicts the double quantum dot charge stability diagram, illustrating how the equilibrium electron occupancy changes with variations in the voltages applied to the plunger gates. In the depicted scenario, the two dots operate independently, and in which the alterations in each gate voltage solely influence the corresponding dot behavior. However, as shown in 1.10(b), if the two dots are capacitive-coupled, an intriguing interplay emerges. In this case, introducing an electron to one dot, not only alters its electrostatic energy but also induces changes in the neighboring dot dynamics due to capacitive coupling. Moreover, the voltage applied to one dot's gate directly impacts the behavior of the other dot through this capacitive interaction. This intricate interdependence underscores the complexity of quantum dot systems and highlights the importance of understanding their coupling mechanisms for precise control and manipulation [16].

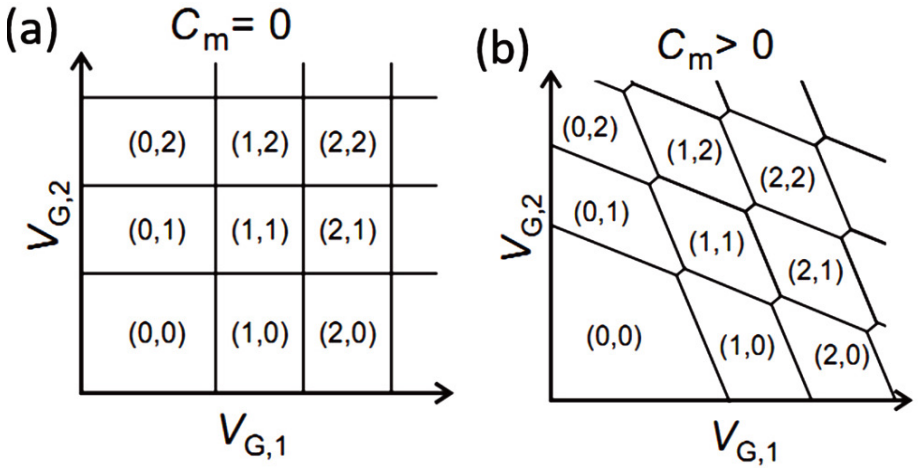

(a) NO COUPLING BETWEEN THE DOTS

(b) COUPLING BETWEEN THE DOTS

Figure 1.10. Figure 1.10(a) represents the Charge Stability Diagram with no coupling between the dots, for this reason, the dots behave independently. In figure 1.10(b) the dots have an interdependence due to the coupling different from zero. Adapted from [17].

Chapter 2

Qubit Semiconductor technologies

This chapter represents an overview of the various semiconductor technology-based approaches for producing qubits. As was previously noted, the focus of this thesis is specifically on quantum dot qubits and the different ways in which they can be encoded. Specifically, this refers to the method of representing quantum information using the quantum states of a system.

2.1 Qubit Implementation

Quantum dots are one of the most interesting ways to define qubits, because of the following advantages:

- **Scalability**: Quantum dots can be fabricated using semiconductor fabrication techniques, making them compatible with existing semiconductor technology. In particular, is fundamental the compatibility with metal-oxide-semiconductor (CMOS) integration techniques [18].

- **Manipulation**: Quantum dots can be handled using techniques such as electrostatic gating, optical excitation, or the application of magnetic fields to control the energy levels of electrons within the dot, thus enabling the encoding and manipulation of quantum information [19].

- **Control**: Individual electrons can be trapped and manipulated within quantum dots, allowing for precise control over their quantum states. This level of control is crucial for performing quantum operations and maintaining coherence, the property that allows quantum information to be processed without decoherence [19].

- **Relatively Long Coherence Times**: it refers to the duration for which a qubit can maintain its quantum state. Quantum dots, in particular spin qubits based on Silicon, can exhibit relatively long coherence times compared to other qubit quantum dot implementations, which is essential for performing complex quantum computations [3].

There are also two alternative methods to create qubits in semiconductors:

- Using dopants, in particular doped silicon, can generate isolated qubits with exceptionally long decoherence times due to the weak spin-orbit coupling [20].
- Optically quantum address defects, for example the diamond nitrogen-vacancy (NV^{-1}) center has become a very suitable qubit candidate from the moment that they can be initialized, manipulated, and measured with high fidelity at room temperature [21].

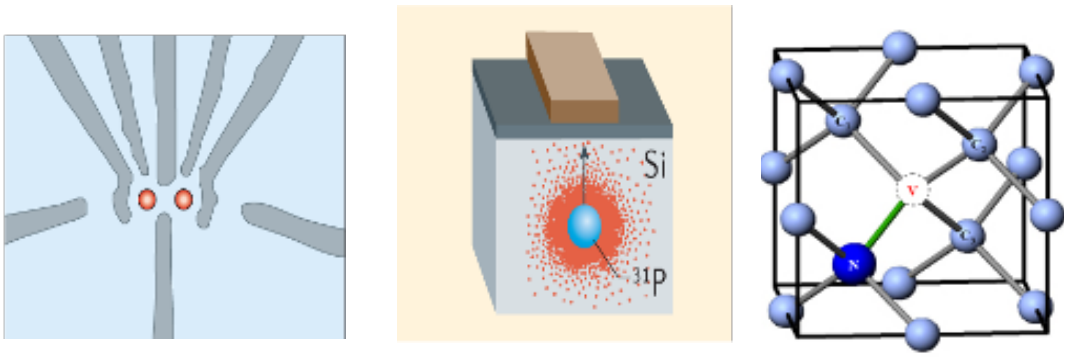

(a) Gated defined QDs (b) Phosphorus dopant atom (c) NV defect

Figure 2.1. Different implementations of semiconductor technology for quantum computing application. Adapted from [22] and [21]

2.2 Quantum Dots Qubit Typologies

Quantum dot qubits can be encoded using different methodologies as it will be described in this section. As previously mentioned in Section 1.1.3, silicon exhibits six degenerate minima. However, the significant in-plane tensile strain in the quantum dot breaks the six degenerate minima into a higher fourfold degenerate level and a lower twofold degenerate level. Additionally, quantum confinement further separates the two lower levels as depicted in [23, 5] and the energy difference between the ground state E_0 and the first excited state E_1 can be defined as valley splitting Δ_v (Figure 2.2). Furthermore, the heterostructure composition influences the value of valley splitting, as described in Section 3.

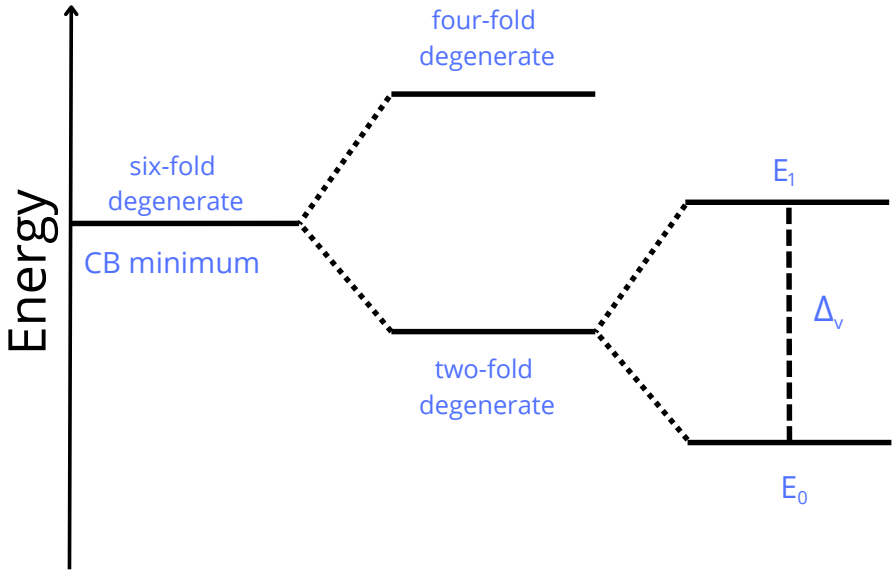

Figure 2.2. Valley splitting in a quantum dot

2.2.1 The Spin-$\frac{1}{2}$ qubit

The use of electron spin is one of the simplest ways to implement a qubit. The spin-$\frac{1}{2}$ qubit relies on the spin of the electron to store quantum information [24]. As mentioned earlier, the strain and the quantum confinement break the sixfold degeneracy of the conduction band minima in silicon, leaving a spin-degenerate ground state.

Hence, this level, which can be occupied by two electrons with different spins, is further split into two levels by the energy E_z, known as the Zeeman energy.

This energy difference is achieved by applying a static magnetic field (see Figure 2.3). Moreover, the lower state of the system depends on the electron spin g-factor of the material of the quantum dot. In fact, for a positive g-factor, the lower state is $|\downarrow\rangle$; otherwise, for negative values the lower state is $|\uparrow\rangle$ [3].

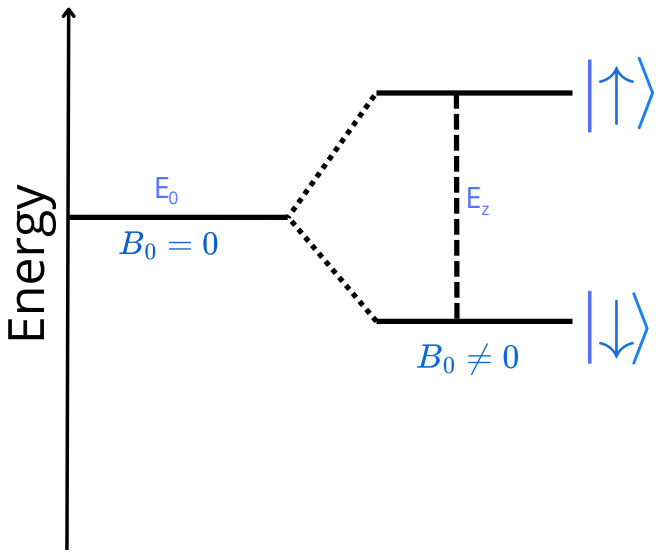

Figure 2.3. The figure describes the split of the spin degeneracy of Silicon, which is characterized by a a positive g-factor.

At this point, it is possible to express the spin system Hamiltonian, written in the $\{|\downarrow\rangle, |\uparrow\rangle\}$ basis as:

$$H = \begin{bmatrix} \frac{Ez}{2} & 0 \\ 0 & -\frac{Ez}{2} \end{bmatrix} \tag{2.1}$$

In this specific type of encoding, each qubit is associated with a quantum dot [18]. To manipulate the information, it is applied precise voltages to the electrical gates, modifying the confinement potential and thereby influencing the electrons' position and energy levels within the quantum dots. This manipulation allows the control of quantum states, enabling the operations necessary for quantum computation. The advantage of this kind of qubit lies in its long decoherence times (tens of microseconds), although it exhibits slower manipulation speeds (tens of nanoseconds).

2.2.2 Charge Qubit

The charge qubit exploits the charge of a physical system to represent quantum information. Specifically, considering a double quantum dot system is employed, the charge corresponds to the movement of an electron between the two dots [25]. Hence, the electron can move between the two dots thanks to a non-zero tunnel coupling. Furthermore, the two states considered are the ground state $|0\rangle$ and the excited state $|1\rangle$. They are usually denoted by $|R\rangle$ and $|L\rangle$ respectively. The system Hamiltonian, in this case, is expressed as:

$$H = \begin{bmatrix} \frac{\epsilon}{2} & t_0 \\ t_0 & -\frac{\epsilon}{2} \end{bmatrix} \tag{2.2}$$

where ϵ is the detuning between the two dots and t_0 is the tunnel coupling.
The considered structure is composed by two dots and an inter-dot barrier, that are controlled by three different gates. Moreover, by adjusting the two dot gates, the detuning between the two dots can be modified while the tunnel coupling can be adjusted through the barrier gate. The qubit's readout can be achieved by employing a charge sensor or by measuring the transport current from the source to the drain. This approach eliminates the need for any conversion steps required in the case of spin qubits [26].
Another significant advantage over charge qubits is the ability for very fast manipulation (tens of picoseconds). However, the decoherence time is not as long as that of spin qubits (tens of nanoseconds).

2.2.3 Singlet-Triplet (ST) qubit

A Singlet-Triplet (ST) qubit is a type of qubit that encodes quantum information using the spin states of two electrons confined within a double quantum dot system. It relies on the concept of singlet and triplet states, where the former is characterized by a total spin quantum number of zero, and the latter by a total spin quantum number of one, allowing spin component values of -1, 0, and 1. Specifically, in the notation, it is crucial to indicate whether the system is in a singlet or triplet state, denoted as $T(NL, NR)$ for a triplet state and $S(NL, NR)$ for a singlet state [27], where NR and NL are the number of the electrons in the right and left dot respectively. From the moment that the triplet state can have three different configurations depending on the total spin number, the notation for the four different states is:

- $T_+(1,1) = |\uparrow\uparrow\rangle$,
- $T_0(1,1) = \frac{1}{\sqrt{2}}(|\uparrow\downarrow\rangle + |\downarrow\uparrow\rangle)$,
- $S(1,1) = \frac{1}{\sqrt{2}}(|\uparrow\downarrow\rangle - |\downarrow\uparrow\rangle)$,
- $T_-(1,1) = |\downarrow\downarrow\rangle$

However, the $S(0,2)$ and $S(2,0)$ states must be considered since they are energetically close to the other four states. Conversely, $T(2,0)$ and $T(0,2)$ states can be disregarded because, according to the Pauli Exclusion Principle, two electrons with the same spin in the same dot must occupy the ground state and the first excited state, that are separated due to valley splitting.

Typically, the encoded states are $S(1,1)$ and $T_0(1,1)$. Specifically, $|0\rangle = S(1,1)$ and $|1\rangle = T_0(1,1)$, and the system Hamiltonian is expressed as:

$$H = \begin{bmatrix} hJ(\epsilon) & \frac{\Delta Ez}{2} \\ \frac{\Delta Ez}{2} & 0 \end{bmatrix} \tag{2.3}$$

where the symbol h represents the Planck constant, the term ϵ is the energy difference (called detuning) between the energy levels of the two quantum dots. Moreover, the parameter ΔEz is the energy difference between the Zeeman energies of the individual dots, and it must be different from zero to implement the Singlet-Triplet qubit. Lastly, $J(\epsilon)$ is called exchange interaction [28], and represents how much overlap between the wavefunctions of electrons in the different dots, which can be tuned through barrier gates and controlling the tunneling coefficient [29]. Moreover, adjusting the detuning parameter ϵ, the exchange interaction can be modified accordingly. This exchange interaction is typically quantified in frequency units, such as Hertz (Hz).

Singlet-triplet qubits may be more susceptible to certain types of errors compared to spin qubits. Managing and mitigating errors, such as charge noise and environmental fluctuations, can be more challenging in singlet-triplet qubit systems [30]. Also, they may have limitations in quantum gate fidelity compared to spin qubits. Achieving high-fidelity quantum operations in singlet-triplet qubits may require additional optimization efforts and they do not have fast manipulation and read-out speed [31] [32]. However, Singlet-triplet qubits can be entirely driven electrically, although they still require a Zeeman energy difference to achieve universal single-qubit control. Consequently, specific qubits, such as the exchange-only qubit, have been implemented. This particular qubit operates solely based on the exchange interaction, eliminating the need for disparate Zeeman energy levels. However, a notable constraint of this approach is its reliance on three electrons distributed across three distinct quantum dots to realize the single qubit [33] [34].

2.2.4 Hybrid qubit

The hybrid qubit stands out for its unique encoding scheme, leveraging both electron positions and spins. It is engineered to exploit the favorable characteristics of both spin qubits, known for their long decoherence times, and charge qubits, recognized for their fast manipulation capabilities. Hence, it is encoded using two eigenstates derived from the spins of three electrons within a double quantum dot system. This innovative qubit configuration was initially build up in a double quantum dot setup within a silicon/silicon-germanium (Si/SiGe) heterostructure environment [35]. The inclusion of a third electron introduces a deviation from purely singlet or triplet states in the quantum system. Consequently, fast electric field manipulation techniques can be employed to rotate the qubit along any desired axis, as demonstrated in [36]. In particular, one of the key distinctions from charge state qubits lies in their enhanced resilience against coherence effects reducing charge fluctuations. Additionally, they offer a more straightforward control methodology compared to spin-1/2 qubits. Finally, in this specific configuration, the qubit states are clearly defined:

- $|0\rangle = |\downarrow\rangle_L |S\rangle_R$ where S stands for singlet state in the right dot
- $|1\rangle = \frac{1}{\sqrt{3}}|\downarrow\rangle_L |T_0\rangle_R + \sqrt{\frac{2}{3}}|\uparrow\rangle_L |T_-\rangle_R$ where T_0 and T_- are two triplet states of the right dot.

This thesis takes into account spin-$\frac{1}{2}$ qubit encoded in silicon-based quantum dot heterostructures due to its scalability, high fidelity, and long coherence times. However, the primary focus of this work is to determine the physical structure parameters necessary for qubit implementation. Consequently, the detailed investigation of the qubit encoding for the various structures is not extensively covered.

Part II

Analysis Description

Chapter 3

Physical description of the three devices

Among all the possible semiconductor heterostructures, this thesis is focused on two different types:

- $Si_{0.7}Ge_{0.3} -^{28} Si - Si_{0.7}Ge_{0.3}$ heterostructure
- $Si -^{28} Si - SiO_2$ heterostructure also called SiMOS structure.

Specifically, simulations are conducted for three different devices. The first two devices consist of double quantum dot structures based on the two distinct heterostructures previously mentioned. The third device is a four-quantum dot structure based on the SiGe heterostructure.

Both heterostructures are developed along the $\hat{z}$-direction, implying that confinement along the $\hat{z}$-direction is generated from the variation in energy gaps energy gaps between materials that trap the electrons in the ^{28}Si layer, as described in Section 1.2. For the $\hat{x}$ and $\hat{y}$ directions, the confinement is achieved through specific applied potentials to the metal gate. Silicon has six degenerate conduction band minima, as discussed earlier. However, quantum dots lift this degeneracy, as detailed in Section 2.2. In particular, in the SiGe-based heterostructure, the splitting is induced by the tensile stress in silicon, as the lattice constant of Si is smaller than of SiGe [37]. In contrast, for the SiMOS structure, the splitting is due to the formation of two-dimensional electron gas quantum confinement across the Si/SiO_2 [100] interface [38, 39]. Furthermore, the lower twofold degenerate level is further split by the electric fields and the confinement in the dot, ultimately yielding a unique spin-degenerate ground state.

It is noteworthy that the energy splitting between the lower twofold degenerate level, known as valley splitting, varies depending on the structure considered. For the SiMOS structure, the energy splitting can oscillate between 0.2 and 0.8 meV [40, 41], whereas for the SiGe structure, the values range between 0.02 and 0.1

eV [42, 43, 44]. The higher splitting in the SiMOS structure is attributed to the sharper potential step at the Si/SiO_2 interface compared to the Si/SiGe interface.

Additionally, an important aspect of these structures is the silicon layer where the electrons are confined. This layer is typically a thin layer of enriched ^{28}Si. Natural silicon contains 4.7% ^{29}Si nuclei, which negatively affect spin coherence. The ^{29}Si nuclei have nonzero nuclear spin, meaning each nucleus interacts with others and with electron spins through hyperfine interactions, leading to very short coherence times. Instead, the 28-isotope of Si has zero net nuclear spin and eliminates this issue. Furthermore, enriched ^{28}Si offers another crucial advantage due to the mass differences between the three stable isotopes [45, 46, 47].

3.1 SiGe Double Quantum Dot Heterostructure

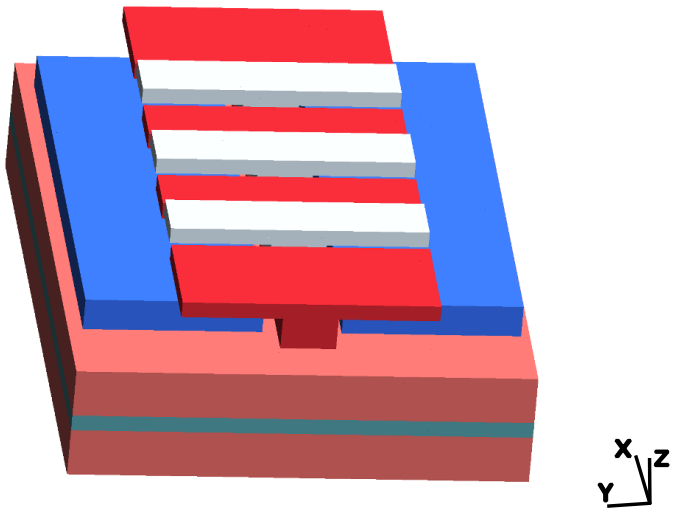

Figure 3.1. Representation of SiGe Double Quantum Dot heterostructure obtained with GMSH [48]. The figure reports the structure of the different gate layers

The heterostructure starts with 300 nm of linearly graded $Si_{1-x}Ge_x$ where the value of x changes from 0 to 0.3. However, our working tool QTCAD is not able to compute automatically the strain from the definition of the material and of the geometry. Therefore, for time computation reasons, this layer cannot be included in the simulation and a strain potential is manually inserted in the code. On top of this, a 30 nm of relaxed $Si_{0.7}Ge_{0.3}$ layer lies below a 10 nm layer of ^{28}Si, that is the quantum layer. However, in the experimental structure reported in [49] the $Si_{0.7}Ge_{0.3}$ thickness is equal to 300 nm, but in order to reduce the memory

usage in the program this layer is reduced. The quantum layer is separated from the 2 nm Si cap by another 30 nm relaxed $Si_{0.7}Ge_{0.3}$ layer. Nevertheless, in the experimental setup, the Si cap oxides before the atomic layer deposition of the top oxide (Al_2O_3) and, for this reason, the Si cap is not considered in our experiment. The device is made by a three-layer gate metal stack which are the Y-gates, the plunger gates, and the barrier gate as reported in Figure 3.1. In the experimental setup, the metal gate is fabricated with a Ti:Pd stack.The 3 nm Ti layer is utilized as an adhesion layer for the Pd layer; consequently, the gates are predominantly composed of Pd. To simplify the structure in the QTCAD simulation, the metal gates are represented by Al_2O_3, and specific boundary conditions are defined at the interface between the oxide structure and the gate region. Each metal layer is separated from the underlying one by 7 nm of oxide. The height of the Y gates is 20 nm, while their width is 106 nm. The extension of dot plungers and barriers over the quantum region is 33 nm along the $\hat{x}$ direction, 33 nm along the $\hat{y}$ direction, and 30 nm along the $\hat{z}$ direction, as depicted in Figure 3.2. The reservoir plungers have the same dimensions as the dot plungers along the $\hat{z}$ and $\hat{y}$ directions, and 66 nm along $\hat{x}$. The barriers and plungers are separated by 7 nm of oxide along the $\hat{x}$ direction. The Y gates are separated from the barriers and plungers by 7 nm of oxide. Finally, there are four ohmic contacts located at the four corners of the structure with a volume of $40 \times 60 \times 45\,nm^3$. This implies that they include the top $Si_{0.7}Ge_{0.3}$, ^{28}Si quantum layer, and 5 nm of the $Si_{0.7}Ge_{0.3}$ below the quantum layer. These ohmic regions are n^+ doped, with a dopant concentration of $5 \times 10^{18}\,cm^{-3}$ [50].

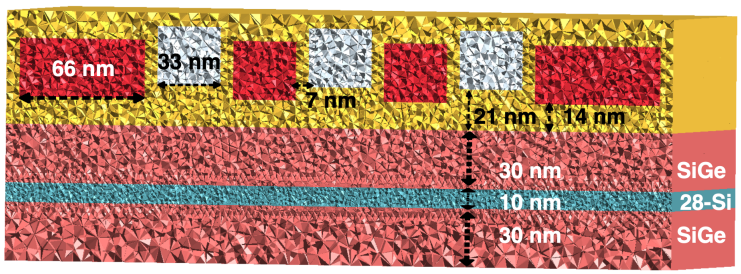

Figure 3.2. SiGe Double Quantum Dot heterostructure obtained with GMSH [48]. The figure reports a cut of the structure along a plane perpendicular to the XY plane in the quantum region

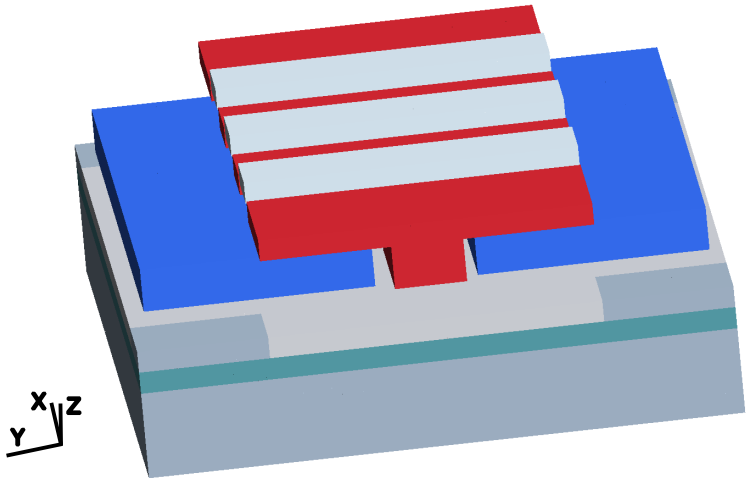

Figure 3.3. SiMOS Double Quantum Dot heterostructure obtained with GMSH [48]. The figure reports the structure of the different gate layers

3.2 SiMOS Double Quantum Dot Heterostructure

The heterostructure begins with a 40 nm Si layer, similar to the SiGe device, which has been reduced from 100 nm to improve computational efficiency. On top of this, a 10 nm isotropically purified ^{28}Si quantum layer is deposited. This is separated from the Al_2O_3 by a 10 nm SiO_2 layer. The device is composed of a three-layer gate metal stack, which includes the Y-gates, the plunger gates, and the barrier gate, as illustrated in Figure 3.3. Each metal layer is separated from the other metal layers by 7 nm of oxide.

The height of the Y gates is 20 nm, while their width is 106 nm. The extension of dot plungers and barriers over the quantum region, as shown in Figure 3.4, is 33 nm along the $\hat{x}$ direction, 33 nm along the $\hat{y}$ direction, and 30 nm along the $\hat{z}$ direction. The reservoir plungers have the same dimensions as the dot plungers along the $\hat{z}$ and $\hat{y}$ directions and 66 nm along the $\hat{x}$ direction. Along the $\hat{x}$ direction, the barriers and plungers are separated by 7 nm of oxide. The Y gates are separated from the barriers and plungers by 7 nm of oxide.

At the four corners of the structure, there are four ohmic contacts with a volume of $40 \times 60 \times 25\,\text{nm}^3$. These contacts include the top Si layer, which replaces the SiO_2 in this area, the 10 nm ^{28}Si quantum layer, and 5 nm of the Si layer below the quantum layer [50].

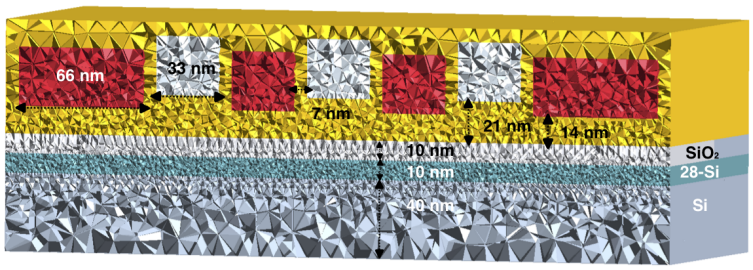

Figure 3.4. SiMOS Double Quantum Dot heterostructure obtained with GMSH [48]. The figure reports a cut of the structure along a plane perpendicular to the XY plane in the quantum region

3.3 SiGe Four Quantum Dot Heterostructure

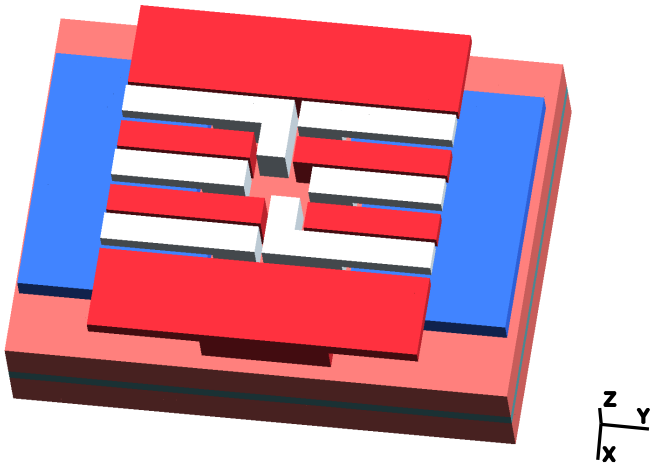

Figure 3.5. SiGe Four Quantum Dot heterostructure obtained with GMSH [48]. The figure reports the structure of the different gate layers

The heterostructure, as described in [51], begins with a 2.5 μm strained relaxed $Si_{0.7}Ge_{0.3}$ layer, which is reduced to 30 nm for computational efficiency, as done in Section 3.1. Since QTCAD cannot automatically compute the strain from the material and geometry definitions, a potential is manually inserted into the code. On top of the $Si_{0.7}Ge_{0.3}$ layer is a 9 nm isotropically enriched ^{28}Si quantum layer, although in the real device, a small concentration of ^{29}Si is still present. This

quantum layer is separated from the 1 nm Si cap by another 30 nm relaxed $Si_{0.7}Ge_{0.3}$ layer, which completes the heterostructure. However, in the experimental setup, the Si cap oxidizes before the atomic layer deposition of the top oxide (Al_2O_3), thus the Si cap is not considered in our experiment. Instead, only 10 nm of Al_2O_3 is used to separate the gate stack from the heterostructure.

The device comprises a three-layer gate metal stack: Y-gates, plunger gates, and barrier gates, as depicted in Figure 3.5. The three gate layers are made of Ti:Pd, but to simplify the structure in the QTCAD simulation, the metal gates are represented by Al_2O_3, with specific boundary conditions defined at the interface between the oxide structure and the gate region. Each metal layer is separated from the underlying one by 5 nm of oxide. The height of the Y gates is 15 nm, while their width varies along the $\hat{x}$ direction. Specifically, the Y gate in the upper region has a width of 127.5 nm from $\hat{x} = 40$ nm to 115 nm, and then it is 112.5 nm wide, whereas in the lower region, the Y gates are 112.5 nm wide from $\hat{x} = 40$ nm to 145 nm, and then 127.5 nm wide.

The extension of dot plungers and barriers over the quantum region, as shown in Figure 3.6, is 20 nm along the $\hat{x}$ direction, 30 nm along the $\hat{y}$ direction, and 30 nm along the $\hat{z}$ direction. However, the right upper barrier and the left lower barrier must separate the dot from the reservoir gates and the two dots along the $\hat{y}$ direction. Therefore, in the simulation, as described in Figure 3.5, they have an L shape, with extensions of 55 nm along the $\hat{y}$ direction and 45 nm along the $\hat{x}$ direction. The reservoir plungers have the same dimensions as the dot plungers along the $\hat{z}$ and $\hat{y}$ directions and 60 nm along the $\hat{x}$ direction, even though they are not aligned as in the two previous cases but are rigidly shifted to accommodate the Y gates. Along the $\hat{x}$ direction, the barriers and plungers are separated by 5 nm of oxide. The Y gates are separated from the barriers and plungers by 5 nm of oxide.

Finally, there are four ohmic contacts at the four corners of the structure, each with a volume of $40 \times 60 \times 44\,\text{nm}^3$. This means they include the top $Si_{0.7}Ge_{0.3}$, the ^{28}Si quantum layer, and 5 nm of the $Si_{0.7}Ge_{0.3}$ below the quantum layer. These ohmic regions are n^+ doped, with a dopant concentration of $5 \times 10^{18}\,\text{cm}^{-3}$.

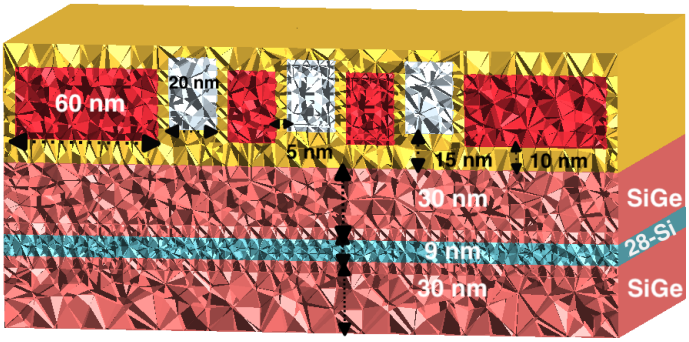

Figure 3.6. SiGe Four Quantum Dot heterostructure obtained with GMSH [48]. The figure reports a cut of the structure along a plane perpendicular to the XY plane in the quantum region

Chapter 4

QTCAD simulation flow

The examination of the heterostructure is conducted using a specialized software known as Quantum Technology Computer-Aided Design (QTCAD), which has been recently developed by Nanoacademic Technologies. Due to QTCAD's absence of an inherent meshing tool, the initial step involves creating the structure and generating the mesh using GMSH. Subsequently, GMSH produces specific files utilized by QTCAD to simulate the device. Through QTCAD, crucial physical parameters of our structures can be extracted, as described in [52]. In fact, it is a Finite Element Method (FEM) based solver created specifically to simulate quantum devices. It offers advanced capabilities for modeling and analyzing quantum systems with high precision, addressing the challenges of quantum device modeling.

4.1 Poisson Equation

The simulation workflow in QTCAD proceeds methodically. Initially, the materials of distinct regions and boundary conditions are defined, referencing the mesh generated by GMSH. Subsequently, the software solves the non-linear Poisson equation, yielding essential parameters such as the conduction band edge and the electrostatic profile of the device, as highlighted in [53]. The non-linear Poisson equation is:

$$-\nabla \cdot (\epsilon \nabla \varphi) = \rho, \tag{4.1}$$

$$\rho = \rho_{semi} + \rho_o \tag{4.2}$$

where the ϵ is the dielectric permittivity of the medium and the φ is the electric potential, ρ is the charge and it can be expressed as the sum of two contributions. The ρ_{semi} is the charge in the semiconductor at the equilibrium

$$\rho_{semi} = e(p - n + N_+ - N_-) \tag{4.3}$$

where e is the elementary charge, n is the electron density, p is the hole density and N_+ and N_- are the densities of ionized donors and acceptors respectively. The equation is defined as non-linear because n and p depend on φ, the variable being solved for. Furthermore, N_+ and N_- may also depend on φ if an incomplete ionization model is considered.
ρ_o is a fixed background volume charge density that can be set by the user.

4.2 Single Particle Schrödinger Equation

Moreover, within regions where classical physics becomes inadequate, the software solves the time-independent Single-Particle Schrödinger equation using the envelope-function approximation (EFA) [54], enabling computations of bound states, their probability density, and energy levels [55]. In particular, it relies on the fact that, within a very small volume, the fast-varying atomistic potential and the slow-varying confinement potential set by the nanostructure are well separated in terms of variation rate. The thesis analysis focuses on the electrons for which QTCAD uses the effective mass approximation [56]. Specifically, the complex interaction of an electron with the periodic potential of the lattice is replaced by considering the electron as a free particle with an "effective mass" that differs from the electron's actual mass in a vacuum. This effective mass accounts for the influence of the periodic potential and makes it easier to analyze the electron's behavior in the material. Furthermore, the electron time-independent Single-Particle Schrödinger Equation is:

$$H(r)F(r) = EF(r), \tag{4.4}$$

$$H(r)F(r) = V_{conf}(r)F(r) + \frac{\hbar^2}{2}\mathbf{k} \cdot M_e^{-1} \cdot \mathbf{k}F(r) \tag{4.5}$$

Considering a single conduction band, the eigenfunctions $F(r)$ and the eigenenergies E are the solutions of the effective Schrödinger equation. V_{conf} is the total confinement potential, $\hbar$ is the reduced Planck constant, M_e^{-1} is the electron inverse mass tensor and $\mathbf{k} = -i\nabla$ is the wave vector operator. Envelope functions substitute the wavefunctions in the conventional Schrödinger equation; however, they do not constitute the complete solution as they do not have the atomistic oscillatory components originating from the crystal potential.

4.3 Lever Arm

Once the Poisson and Schrödinger equations are solved for the reference potential configuration, it is possible to compute an important quantity known as the lever arm. This unitless coefficient quantifies the extent to which a gate, denoted as G,

can modify the electrochemical potentials μ of a quantum dot:

$$\mu = \mu_0 - e\alpha_G V_G \tag{4.6}$$

where e > 0 is the elementary charge and μ_0 is the dot's electro-chemical potential when $V_G = 0$.Taking into account that the electro-chemical potential is defined as [16]:

$$\mu = E_{tot}(N) - E_{tot}(N-1) \tag{4.7}$$

where $E_{tot}(N)$ is the total energy of the dot in N-electrons ground state, and considering the constant interaction model [57], the lever arm is defined as:

$$\alpha_G = -\frac{C_{0G}}{C_\Sigma} \tag{4.8}$$

In QTCAD, C_{0G} represents the capacitance between the dot and the gate, while C_Σ denotes the self-capacitance of the dot. Nevertheless, it is possible to compute the lever arm explicitly without directly calculating these capacitances. By analyzing the electronic configuration's response to changes in gate bias, the lever arm can be calculated through a straightforward linear fit of this response.

Additionally, QTCAD features a module to automatically compute the lever arm. Specifically, the software solves the non linear Poisson equation for various bias values of V_G, with the other gates held fixed. Subsequently, it solves the Single-particle Schrödinger Equation for each bias configuration. Finally, a linear fit is performed on the different ground-state energies obtained from the solution of the Single-particle Schrödinger Equation.

4.4 Multi-particle Schrödinger Equation

In scenarios where the structure is made by multiple quantum dots, a many-body analysis becomes indispensable. Many aspects can be captured only through a multi-particle simulation approach. Single-particle solvers can describe quantum-mechanically confined carriers and classical gases but interactions between confined particles are not modeled at a quantum-mechanical level [58]. For this reason, this approach considers in an approximated way exchange and correlation effects that come from a quantum-mechanical analysis of the Coulomb interaction. QTCAD uses a many-body solver grounded in the exact-diagonalization approach, enabling an accurate depiction of exchange and correlation effects [59]. This technique includes the exchange and the correlation effects exactly, in contrast with the Hartree–Fock and similar method [60] a mean-field approximation is implied.
Although many-body analyses may be time-intensive, QTCAD is engineered to efficiently simulate semiconductor systems used to implement qubits, typically involving a limited number of electrons and yielding meaningful results within a few minutes.

Considering second quantization and using the effective mass approach used in Equation (4.5), the Hamiltonian for N conduction electrons, that are coupled through Coulomb interaction, is:

$$H = \sum_{i\sigma} \epsilon_{i\sigma} \hat{c}^{\dagger}_{i\sigma} c_{i\sigma} + \frac{1}{2} \sum_{ijkl,\sigma\sigma'} V_{ijlk} \hat{c}^{\dagger}_{i\sigma} \hat{c}^{\dagger}_{j\sigma'} \hat{c}_{k\sigma} \hat{c}_{l\sigma} \tag{4.9}$$

where $\hat{c}_{i\sigma}$ is the fermionic operator which annihilates an electrons of spin σ in the i-basis state, $\hat{c}^{\dagger}_{i\sigma}$ is the fermionic operator that creates an electrons of spin σ in the i-basis, $\epsilon_{i\sigma}$ is the energy of single particle eigenstate with orbital index i and spin index σ and V_{ijkl} is the Coulomb integral of the basis set [61].
In quantum mechanics, a Fermi gas confined within a potential can be effectively described by the Fermi-Hubbard model. Given that double quantum dots with multiple electrons constitute a many-body system of fermions, employing the Fermi-Hubbard model offers a simplified yet effective approach to capturing the intricate physics involved [62]. Therefore, it becomes feasible to model the Equation 4.9 using the Fermi-Hubbard model:

$$H_D \approx \sum_{i\sigma} \epsilon_{i\sigma} n_{i\sigma} + \sum_{i} \frac{U_i}{2} n_i (n_i - 1) + \frac{1}{2} \sum_{j, j \neq i} V_{ij} n_i n_j, \tag{4.10}$$

where the particle operators $n_i = \sum_{\sigma} n_{i\sigma}, n_{i\sigma} = c^{\dagger}_{i\sigma} c_{i\sigma}$ and the Coulomb interaction energies U_i and V_i are introduced. The main advantage of these approximations is that the number of Coulomb integrals to evaluate for n_{states} single-particle states scales like $\mathcal{O}(n^2_{\text{states}})$ instead of $\mathcal{O}(n^4_{\text{states}})$ when overlap terms are included. Furthermore, considering n_{states} states with a degeneracy n_{degen} and a single-body envelope function $F_i(r)$, QTCAD's many-body solver reduces the Hamiltonian of (4.9) into $N_{max} = n_{states} \times n_{degen} + 1$ many-body subspaces by first evaluating Coulomb integrals and then diagonalizing it. Consequently, many-body eigensolutions are determined within each subspace, providing a numerical solution to the many-body problem when N_{max} is sufficiently small (typically on the order of 10 electrons). However, to obtain important physical heterostructure parameters to precisely model the qubit, only a small number of electrons is necessary.

4.5 Transport analysis

Once the many-body solver is set up using QTCAD, it becomes feasible to describe quantum transport [61]. QTCAD models carrier transport by conceptualizing the device as a junction. Specifically, the quantum region interfaces with two leads (source and drain), and the device may incorporate several gates that regulate the potential confinement within the quantum region. Carrier transport thus proceeds from the source towards the drain via sequential tunneling through the quantum dot region.

Through QTCAD's transport analysis, one can compute Coulomb Peaks, Coulomb Diamonds, and Charge Stability Diagrams, which are fundamental in illustrating the single-electron regime. Within QTCAD's transport solver the many-body characterization of the device is obtained by adding the coupling between the quantum region and the leads, that is generated from tunneling events:

$$H = \sum_{i\sigma} \epsilon_{i\sigma} \hat{c}^{\dagger}_{i\sigma} c_{i\sigma} + \frac{1}{2} \sum_{ijkl,\sigma\sigma'} V_{ijlk} \hat{c}^{\dagger}_{i\sigma} \hat{c}^{\dagger}_{j\sigma'} \hat{c}_{k\sigma} \hat{c}_{l\sigma} + \sum_{\mathbf{k}L} \epsilon_{\mathbf{k}L} c^{\dagger}_{\mathbf{k}L} c_{\mathbf{k}L} + \sum_{\mathbf{k}L,i\sigma} (t^{*}_{\mathbf{k}L,i\sigma} c^{\dagger}_{\mathbf{k}L} c_{i\sigma} + H.c.) \tag{4.11}$$

the first two terms correspond to many-body Hamiltonian introduced in Equation (4.9), the third term is the free Hamiltonian of source and drain with $\epsilon_{\mathbf{k}L}$ the energy of a lead $L \in [D, S]$ eigenstate with wave vector $\mathbf{k}$. The last term of the equation describes the tunneling between the device and the leads, with $t_{\mathbf{k}L,i\sigma}$ the tunneling matrix element between the single electron eigenstates $(i\sigma)$ of the quantum region and the eigenstates $\mathbf{k}$ of the lead L. In the QTCAD transport regime, the many-body device Hamiltonian is solved using the exact diagonalization method and the interactions between the source, the drain and the dot, modeled as a weak perturbation. Moreover, transport phenomena are described using the master equation [61].

$$\dot{p}_m = -p_m \sum_{n \neq m} \gamma_{nm} + \sum_{n \neq m} p_n \gamma_{mn} = 0, \tag{4.12}$$

Which is assumed to be in a steady-state regime. The indices m and n denote the different eigenstates of the system, p_m represents the occupation probability of state m, and γ_{mn} is the total transition rate from n to m, which is described as:

$$\gamma_{mn} = \Gamma^{\mathrm{S}}_{n \to m} + \Gamma^{\mathrm{D}}_{n \to m} \tag{4.13}$$

$\Gamma^{\mathrm{S(D)}}_{n \to m}$ represents the contribution to the transition rate attributed to the source (drain) lead. Lastly, the charge current, corresponding to electrons entering the device from the source, is:

$$I^{\mathrm{S}} = -e \sum_{\alpha\beta} p_\alpha \left[\Gamma^{\mathrm{S}}(\alpha_N \to \beta_{N+1}) - \Gamma^{\mathrm{S}}(\alpha_N \to \beta_{N-1}) \right] \tag{4.14}$$

in which $\Gamma^{\mathrm{S}}(\alpha_N \to \beta_{N+1})$ is the transition rate associated with releasing an electron from the lead into the device, while $\Gamma^{\mathrm{S}}(\alpha_N \to \beta_{N-1})$ is the transition rate associated with realizing an electron from the device into the lead. Both transition rates are

defined using Fermi's golden rule [63], as follows:

$$\begin{aligned}
&\Gamma^L(\alpha_N \to \beta_{N+1}) \\
&\quad = n_F\left(\frac{E_\beta^{N+1} - E_\alpha^N - \mu_L}{k_B T}\right) \\
&\qquad \sum_{\mu\nu} \langle \beta_{N+1} | c_\mu^\dagger | \alpha_N \rangle \, \Gamma_{\mu\nu}^L (E_\beta^{N+1} - E_\alpha^N) \, \langle \alpha_N | \, c_\nu \, | \beta_{N+1} \rangle \,, \\
&\Gamma^L(\alpha_N \to \beta_{N-1}) \\
&\quad = \left[1 - n_F\left(\frac{E_\alpha^N - E_\beta^{N-1} - \mu_L}{k_B T}\right)\right] \\
&\qquad \sum_{\mu\nu} \langle \alpha_N | c_\mu^\dagger | \beta_{N-1} \rangle \, \Gamma_{\mu\nu}^L (E_\alpha^N - E_\beta^{N-1}) \, \langle \beta_{N-1} | \, c_\nu \, | \alpha_N \rangle
\end{aligned} \tag{4.15}$$

where $L \in \{\mathrm{S}, \mathrm{D}\}$ is the lead index (source or drain), μ and ν are indices that describe the orbital-state and degeneracy of the single-electron basis states respectively, E_α^N is the energy of the many-body eigenstate $|\alpha_N\rangle$, μ_L is the chemical potential of the lead L, $n_F(x)$ is the Fermi–Dirac distribution and is $\Gamma_{\mu\nu}^L(E)$ is the broadening function

Using the charge conservation concept, it is possible to additionally introduce the charge current I^{D} associated with electrons entering the device from the drain:

$$I^{\mathrm{S}} + I^{\mathrm{D}} = 0 \tag{4.16}$$

4.5.1 Particle Addition Spectrum

The charge stability diagram, as defined in Section 1.4, illustrates the charge configuration of the quantum dot system as a function of plunger gate biases, while accounting for sufficiently small source-drain voltages (reflecting thermal equilibrium of quantum dots with the leads). Therefore, a fundamental quantity for thesis analysis is the total number of particles in the system. Considering a constant temperature T and chemical equilibrium with leads at chemical potential μ, the average number of particles is given by:

$$\langle N \rangle = k_B T \frac{\partial \log \mathcal{Z}}{\partial \mu} \tag{4.17}$$

where k_B is the Boltzmann Constant and $\mathcal{Z}$ is the grand partition function, defined as:

$$\mathcal{Z} = \mathrm{Tr}\left[\exp\left(-\frac{H - \mu N}{k_B T}\right)\right] \tag{4.18}$$

Furthermore, changes in the total number of particles correspond to peaks observed in the particle addition spectrum as defined by [62]:

$$\frac{\partial\langle N\rangle}{\partial\mu} = \frac{\langle N^2\rangle - \langle N\rangle^2}{k_B T} \tag{4.19}$$

Hence, the particle addition spectrum as a function of gate bias configurations gives diagrams in which non-zero values indicate configurations that modify the total particle number.

4.6 QTCAD Simulation Complications

4.6.1 Potential configuration and Non-linear Poisson equation convergence

One of QTCAD's primary drawbacks is the slow convergence of the non-linear Poisson solution under a small error threshold. Specifically, it is necessary to define an optimal mesh in GMSH, which contains a significant number of nodes both inside and close to the quantum layer. However, as shown below, QTCAD's iterative solution to the Poisson equation refines the mesh at each iteration by adjusting certain parameters. Additionally, a specific potential configuration needs to be established to achieve the proper confinement of the dots. Finding the right configuration to ensure that the quantum dots are precisely localized in the correct spot requires many simulations. Currently, there is no established procedure for determining the precise potential arrangement.

4.6.2 Plunger gate Tuning

An ideal double quantum dot structure would exhibit perfect symmetry if the same voltage were applied to both plunger gates. However, due to mesh asymmetries, the potential profile becomes asymmetric, leading to an unequal distribution of the wavefunction between the two dots. To achieve a symmetric configuration, an offset voltage is applied to the dot where the wavefunction of the first excited level is predominantly distributed. In fact, to ensure the wavefunction is evenly distributed over both dots, the energy of the first excited level must decrease. Specifically, the offset voltage is determined by adding to it the difference between the ground state and the first excited level until this difference falls below a certain threshold. The thresholds are different between the two structures, it has been defined as 3×10^{-6} eV for the SiMOS, while for the SiGe structure has been fixed as 1×10^{-7} eV. However, if the offset voltage is too high, the ground state wavefunction becomes predominantly distributed in the dot where the offset voltage is applied. Consequently, further increasing the offset voltage leads to an increased splitting between the two levels.

To address this issue, if the difference between the two levels increases compared to the previous value, the energy splitting is subtracted from the offset voltage. Consequently, the offset voltage converges to a specific value that results in a symmetric distribution of potential, ensuring that the energy splitting remains below a certain threshold. However, as the behavior approaches the two thresholds, it becomes random. This emphasizes the need for constant monitoring to determine the offset that yields the most symmetric configuration. Mesh asymmetry also affects the potential profile in the case of four dots. In this scenario, potential corrections are applied to three of the four dots to ensure that the wavefunction is well distributed across all four dots. Therefore no standard procedure is defined also in this circumstance.

Part III

Implementation

Chapter 5

Double Quantum Dots Analysis

This chapter aims to present all the results obtained from the simulation of the double dot heterostructure using the QTCAD software. Specifically, this chapter begins with the results obtained from solving the Poisson and Schrödinger equation and subsequently progresses to the main focus: the transport analysis. From the moment that the analysis Poisson and Schrödinger equation of this structure is already performed in [50].

5.1 SiGe Double Quantum Dot heterostructure Poisson-Schrödinger Analysis

Considering the structure previously described some parameters are defined to perform the following analysis. The temperature is fixed at 15 mK, and the dopant concentration is set to $N_D = 1 \times 10^{18}\,\mathrm{cm}^{-3}$, with complete ionization assumed. Additionally, the metal workfunction is considered to be:

$$\phi_m = \chi_{Si_{0.7}Ge_{0.3}} + \frac{E_{g-Si_{0.7}Ge_{0.3}}}{2} \tag{5.1}$$

where $\chi_{Si_{0.7}Ge_{0.3}}$ and $E_{g-Si_{0.7}Ge_{0.3}}$ are the electron affinity and the band gap energy of $Si_{0.7}Ge_{0.3}$ respectively. Regarding the mesh obtained in GMSH, the node element size ranges from 4 nm in the bottom $Si_{0.7}Ge_{0.3}$ layer to 2 nm above and below the quantum layer, till 1 nm inside the quantum layer. Finally, it ranges from 4 nm to 2 nm inside the upper three gate layers. Furthermore, the applied voltages are

introduced by setting Dirichlet boundary conditions within the FEM solver:

$$\begin{aligned} V_{Y1} &= 290\,\text{mV} \\ V_{Y2} &= 290\,\text{mV} \\ V_{PL} &= 780\,\text{mV} \\ V_{PR} &= 780\,\text{mV} \\ V_{BL} &= -200\,\text{mV} \\ V_{BM} &= -150\,\text{mV} \\ V_{BR} &= -200\,\text{mV} \\ V_{RL} &= 600\,\text{mV} \\ V_{RR} &= 600\,\text{mV} \end{aligned} \tag{5.2}$$

where V_{Yi} is the applied voltage to the i-Y gate, V_{Pi} is the applied voltage to the i-Plunger gate, V_{Bi} is the applied voltage to the i-Barrier gate, and V_{Ri} is the applied voltage to the i-Reservoir gate. Here, R, L, and M respectively stand for right, left, and inter-dot. Moreover, considering what was discussed in Section 4.6.2, an offset voltage of 593.44 µV is applied to the Right Dot Plunger, obtaining a symmetric potential profile. Finally, from the moment that no strain can be simulated in QTCAD, as mentioned in Section 3.1, a fictitious potential equal to -0.146 V is applied to the Si quantum layer to align the minimum of the conduction band of $Si_{0.7}Ge_{0.3}$ with the ^{28}Si one.

5.1.1 Non-linear Poisson Equation

The initial simulation results are derived from solving the non-linear Poisson equation. Specifically, an iterative approach is employed to solve the non-linear Poisson equation, where the mesh is refined at each iteration until the error falls below a certain threshold, set to 1×10^{-7}. The refinement is optimized by setting specific parameters in the simulation code.

One of the significant results obtained from solving the Poisson equation is the Conduction Band minimum inside the quantum layer. It can be observed in Figure 5.1(a), where the dark blue regions represent the four ohmic contacts (n+ doped area), while the light blue regions on the left and right represent the two reservoir gates. Furthermore, from the representation of the conduction band minimum, it is evident how well-defined the two quantum dots are inside the quantum layer. However, the Poisson solution also provides insights into the classical electron population within the quantum layer, specifically at $z = 35$ nm, as depicted in Figure 5.1(b). In this representation, the quantum dots are not discernible as a uniform distribution is observed, except for the four n+ doped regions (dark red) and the reservoir regions (light blue). This underscores the inadequacy of a classical analysis of carriers within the quantum layer, emphasizing the necessity of employing a quantum mechanics approach.

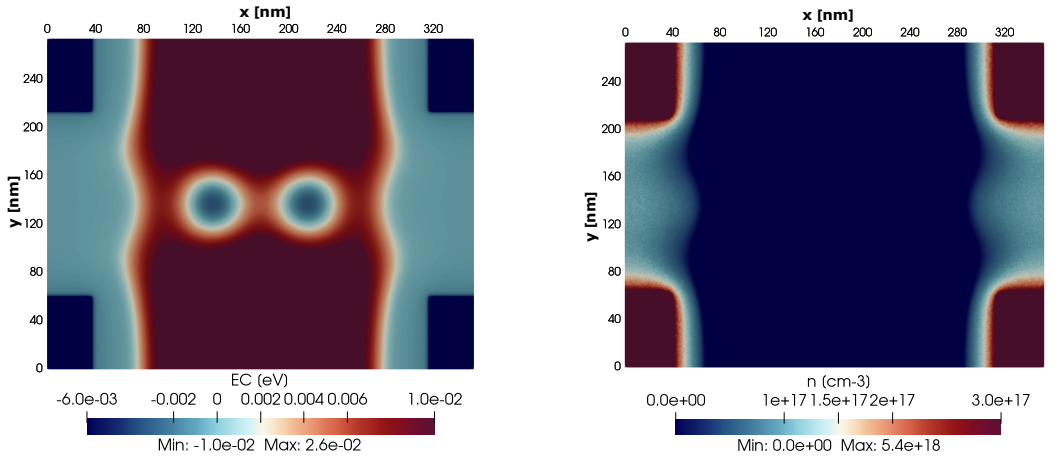

(a) SiGe Double Quantum Dot heterostructure Conduction Band Minimum

(b) SiGe Double Quantum Dot heterostructure classical electrons density

Figure 5.1. Various properties of the SiGe Double Quantum Dot heterostructure obtained by solving the Non-Linear Poisson Equation in QTCAD [64]. On the left 5.1(a), the SiGe Double Quantum Dot heterostructure Conduction Band Minimum in the xy plane considering $z = 35$ nm, hence located inside the quantum layer, is obtained by solving the Non-Linear Poisson Equation in QTCAD [64]. On the right 5.1(b), the SiGe Double Quantum Dot heterostructure classical electrons density in the xy plane considering $z = 35$ nm, hence located inside the quantum layer, is obtained by solving the Non-Linear Poisson Equation in QTCAD [64].

5.1.2 Single-Particle Schrödinger Equation

Considering the classical physics inadequacy, a quantum mechanics approach is employed by solving the Single-Particle Schrödinger equation. Specifically, the Schrödinger equation is solved in the quantum region, which has the following dimensions:

- along the $\hat{x}$ axis, from $x = 93.5$ nm to 259.5 nm
- along the $\hat{y}$ axis, from $y = 60$ nm to 213 nm
- along the $\hat{z}$ axis, from $z = 25$ nm to 45 nm

In this case, the threshold error is set to 1×10^{-9}. Solving the Single-Particle Schrödinger Equation allows to determine the eigenstates and eigenenergies. Specifically, Figure 5.2(a) and Figure 5.2(b), show the cuts on the xy plane inside the quantum layer, depicting the bonding and antibonding eigenfunctions, revealing an equal distribution of the wavefunction over the dots. Additionally, Figure 5.3 lists the eigenenergies of the first five eigenstates. Moreover, as described in Section 4.3, the lever arm matrix results have been obtained in simulation, as reported in Table

5.1, and they can be employed for the tunneling coefficinet analysis as function of the inter-dot barrier gate voltage. Finally, by considering the eigenenergies of Figure 5.3, it is possible to compute an approximation of the tunneling coupling between the dots [65]:

$$t_0 \approx \frac{E_1 - E_0}{2} = 300 \text{ neV} \implies 72.53 \text{ MHz} \tag{5.3}$$

where E_1 and E_0 are the first excited level energy and the ground state level energy respectively with zero detuning. The results obtained shows the behavior of the tunneling coefficient as function of the inter-dot barrier voltage, while keeping the other gate voltages fixed, as represented in Figure 5.4. In fact, with a high inter-dot barrier, the splitting of the levels decreases ($E_1 \approx E_0$), resulting in a low tunneling coefficient. Otherwise, a low inter-dot barrier means high splitting between E_1 and E_0, hence a high tunneling coefficient. As done for the eigenstate representation, the mesh asymmetries must be taken into account when the inter-dot barrier voltage is modified.

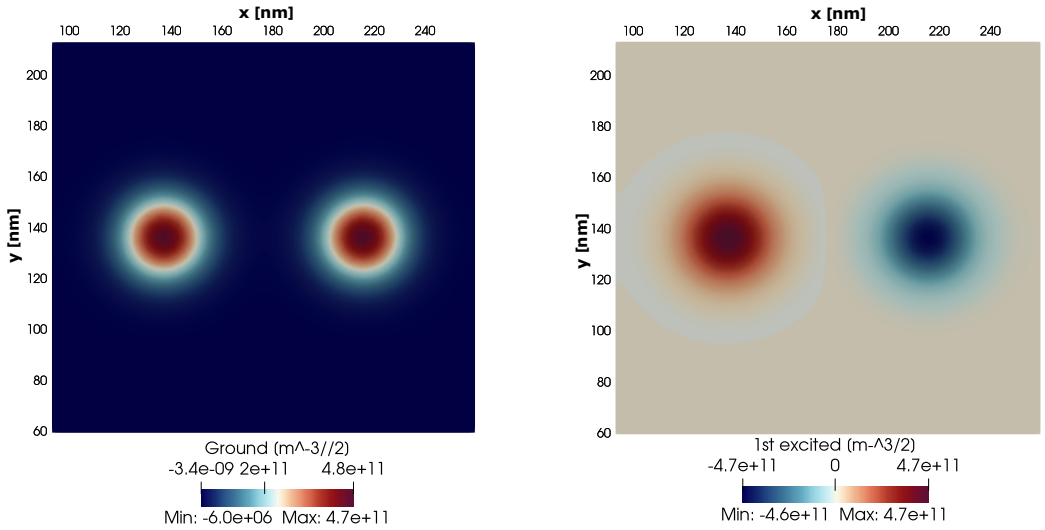

(a) Bonding single-particle eigenfunction in the xy plane

(b) Antibonding single-particle eigenfunction in the xy plane

Figure 5.2. Single-particle eigenfunction in the xy plane for the SiGe Double Quantum Dot heterostructure. On the left 5.2(a), the Bonding single-particle eigenfunction located at $z = 35$ nm, hence inside the quantum layer. On the right 5.2(b), the Antibonding single-particle eigenfunction located at $z = 35$ nm, hence inside the quantum layer. Both are obtained by solving the Single-Particle Schrödinger Equation in QTCAD [64].

Energy Level	Energy [meV]
0	3.27559
1	3.27619
2	6.2927
3	6.31264
4	6.48457

Figure 5.3. Eigenenergies for the first five states of the SiGe Double Quantum Dot heterostructure obtained by solving the Single-Particle Schrödinger Equation in QTCAD [64].

Energy Level	α_{PL}	α_{BM}	α_{PR}
0	7.773×10^{-2}	2.440×10^{-2}	7.770×10^{-2}
1	2.083×10^{-2}	2.439×10^{-2}	2.075×10^{-2}
2	5.054×10^{-2}	2.528×10^{-2}	5.220×10^{-2}
3	4.438×10^{-2}	2.497×10^{-2}	4.263×10^{-2}
4	7.453×10^{-2}	2.311×10^{-2}	5.614×10^{-2}

Table 5.1. Lever Arm matrix of the SiGe Double Quantum Dot heterostructure for the first five states, considering the two plungers gate and the inter-dot barrier gate of obtained by solving the Single-Particle Schrödinger Equation in QTCAD [64]. The voltage increment, to compute the Lever Arm matrix, is approximately equal to 100 µV

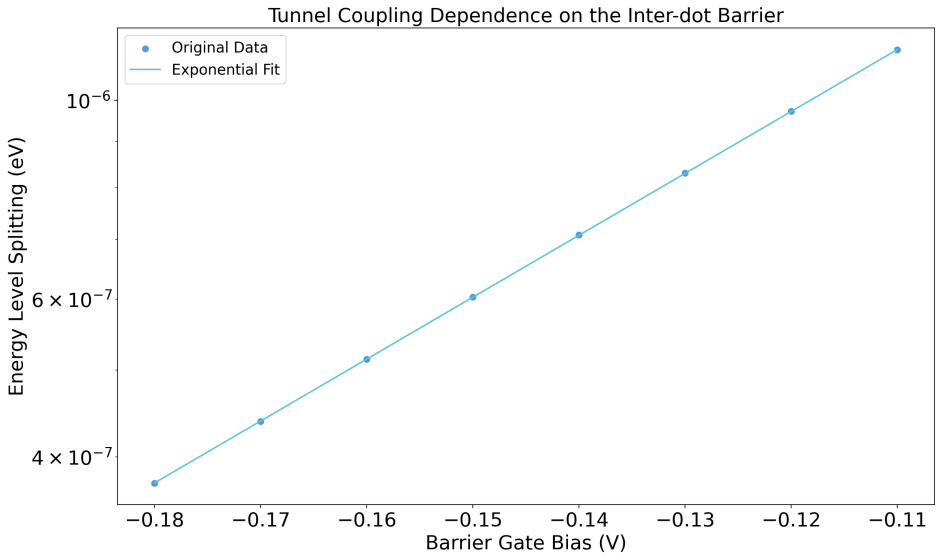

Figure 5.4. E_1 and E_0 splitting energy by changing the inter.dot barrier voltage for the SiGe heterostructure obtained in QTCAD [64].

5.2 SiGe Double Quantum Dot heterostructure Transport Analysis

Transport analysis is fundamental for understanding how electrons move between the quantized energy levels of quantum dots, and this information is crucial for optimizing the performance of qubits based on quantum dots. In a multiple quantum dot scenario, solving the Single-Particle Schrödinger Equation alone is insufficient. Therefore, a multi-particle solver is implemented, as described in Section 4.4. Then, a comprehensive transport analysis of our structure is performed once the QTCAD many-body solver is set up.

5.2.1 Coulomb Peaks

Coulomb peaks are a series of sharp peaks observed in the current of a quantum dot system as a function of gate voltage or bias voltage. These peaks are not related to various single-electron eigenstates (orbital and spin), rather the distance between two peaks corresponds to the energy required for the quantum dot to transition from a state with N electrons to a state with N+1 electrons. Since a 1D analysis is necessary to compute the Coulomb Peaks, our structure must be reduced to a single dot. Two solutions are explored: the first entails removing the inter-dot barrier by applying the same potential both the inter-dot barrier gate and the plunger gates,

while the second involves modifying the structure in GMSH. This modification is depicted in Figure 5.5, where the inter-dot barrier gate is eliminated leaving only a single large dot with a plunger gate.

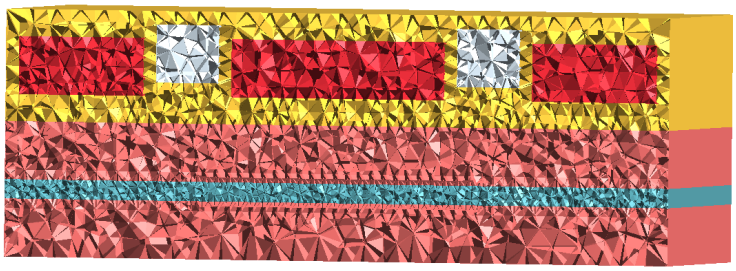

Figure 5.5. SiGe modified Heterostructure obtained in GMSH [48] performing a cut along a plane perpendicular to the xy plane. Now, the structure has only one Dot Plunger in red, maintaining the other structure parameters are the same

Moreover, the positions of the peaks are located at:

$$\Phi_{bias} = \frac{\mu(N)}{\alpha e} \tag{5.4}$$

where α is the lever arm, that for simplicity in this simulation is considered equal to 1, μ is the electrochemical potential defined in Equation 4.7, and e is the elementary electron charge.

As outlined in Section 4.5, the device is treated as a junction, therefore the Coulomb Peaks are obtained by calculating the current entering the device while varying the plunger dot voltage between -0.04 V and 0.05 V vanishing source-drain voltage (in this case $V_{DS} = 100$ µ V, as described by Equation 4.14). Two states with a degeneracy of two are specifically considered, setting the temperature to 1 K and the broadening of the energy level to 10 Hz using a constant function to describe it.

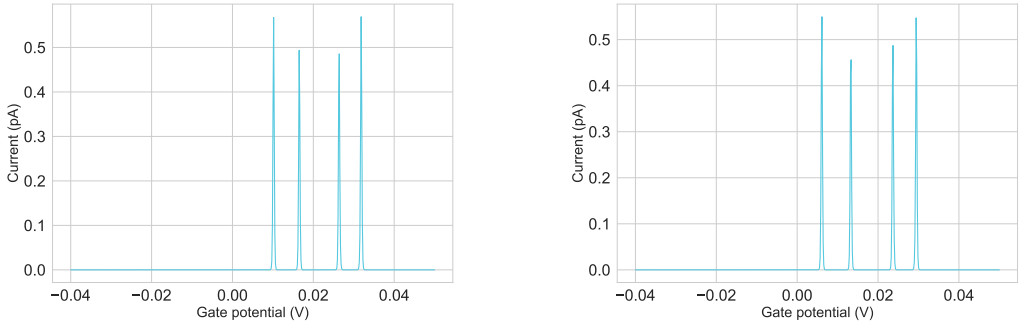

(a) Coulomb Peaks obtained in QTCAD [64], by applying the same potential of the two dot plungers to the inter-dot barrier.

(b) Coulomb Peaks obtained in QTCAD [64] by modifying the structure in GMSH

Figure 5.6. Coulomb Peaks for the SiGe Heterostructure obtained in QTCAD [64]. On the left 5.16(a), Coulomb Peaks for the SiGe Heterostructure with the same potential applied to the two dot plungers and the inter-dot barrier. On the right 5.16(b), Coulomb Peaks for the SiGe Heterostructure with a modified structure in GMSH, reduced to one single big dot.

Despite considering only two states, four peaks are observed in both Figure 5.6(a) and Figure 5.6(b). This occurs because the peaks that you observe are not related to various single-electron eigenstates (orbital and spin) but rather to the energy required for the quantum dot to go from a state with N electrons to a state with N+1 electrons. For this reason in the absence of a magnetic field, the energy required to go from 0 to 1 electron is equal to the single-electron orbital ground state energy, meaning that states with different spin are indeed coincident. Consequently, to go from 1 to 2 electrons, the energy required would be the difference between the single-electron ground state and the two-electron ground state, and so forth. Moreover, considering the Constant Interaction model [16] that is a very rough approximation that does not capture all the complexity of the many-body physics observed in exact diagonalization (the technique used in QTCAD), but still provides some qualitative understanding of the underlying physics. In the CI model, the difference between chemical potentials with N and N+1 electrons is:

$$E_{\text{add}}(N) = \mu(N+1) - \mu(N) = E_c + \Delta E \tag{5.5}$$

where $\mu(N+1)$ is the electrochemical potential with N+1 electrons, $\mu(N)$ is the electrochemical potential with N electrons, ΔE is the difference between two discrete single-electron levels and $E_C = e^2/C$ is the charging energy, with $C = C_S + C_D + C_G$, where C_S, C_D and C_G are the source, drain, and gate capacitances, respectively. Hence, even for degenerate orbital levels ($\Delta E = 0$), non-coincident peaks are present because of the charging energy E_C that arises from Coulomb interactions

between the electrons in the quantum dot. Furthermore, the different peak heights, adopting Equation 4.14, are due to the different values of the many-body transition rates for the various states obtained through Equation 4.15. In fact, even if the broadening function (single-body transition rates) is assumed constant, the many-body transition rates are not, resulting in varying peak heights. Both solutions yield similar results. However, minor discrepancies may arise due to variations in the potential profile obtained in the two solutions, as shown in Figure 5.7(a) and Figure 5.7(b). Finally, the voltage applied to the dot plunger is reduced to 0.5 V compared to the double quantum dot configuration. This adjustment prevents the formation of an excessively deep dot, which could potentially lead to issues.

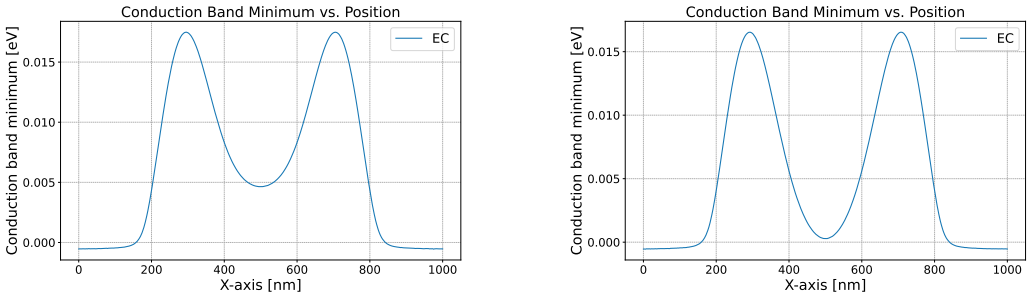

(a) SiGe Heterostructure Conduction Band Minimum with modified V_{BM}

(b) SiGe Heterostructure Conduction Band Minimum with GMSH modified structure

Figure 5.7. the Conduction Band Minimum for the SiGe Heterostructure obtained in QTCAD [64]. On the left 5.7(a), the Conduction Band Minimum for the SiMOS Heterostructure with modified V_{BM}. On the right 5.7(b) the Conduction Band Minimum for the SiMOS Heterostructure with GMSH modified structure. Both images are cuts along the $\hat{x}$ axis at $y = 136.5$ nm and $z = 35$ nm.

5.2.2 Coulomb Diamonds

The Coulomb Diamonds represent the relationship between differential conductance, source-drain voltage, and gate voltage. Similar to the Coulomb peaks scenario, a one-dimensional analysis is necessary, employing the same methodologies previously used to simplify the structure to a single dot. Additionally, an approximation is introduced: rather than computing the full differential conductance, only the difference between the extreme current values at different potential configurations are considered. Specifically, the current values for each bias configuration are obtained by sweeping both the gate voltage and the source-drain bias using Equation 4.14. As for the Coulomb Peaks, two states with degeneracy two are considered in the analysis. Moreover the source-drain voltage sweeps between -8 mV and 8 mV, the plunger dot gate voltage sweeps -0.06 V and 0.05 V, the broadening is considered equal to 1 Hz, the temperature is set to 1 K and for simplicity the lever

arm of the gate is considered equal to one. The resulting Coulomb Diamond patterns, depicted in Figure 5.8(a) and Figure 5.8(b), show regions of blockade where the number of electrons is constant. Similarly to the Coulomb Peaks case, the results are comparable for the two methods used to reduce the structure to a single dot. However, minor discrepancies arise due to differences in the potential profile. Furthermore, the obtained results reveal five diamonds along the $\hat{x}$-axis, representing five Coulomb blockade regions where the number of electrons is fixed. It is worth noting that even without applying a magnetic field, five blockade regions are present. This is because Coulomb Diamonds are not related to the single-particle eigenstates but to the system electron number. Furthermore, the central diamond is larger compared to the two adjacent ones because it separates two different states, whereas the other two separate the same state with different numbers of electrons. Finally, following the approach used for the Coulomb Peaks, the voltage applied to the plunger gate is reduced to 0.5 V compared to the double quantum dot configuration to avoid the formation of an excessively deep dot, which could potentially cause issues.

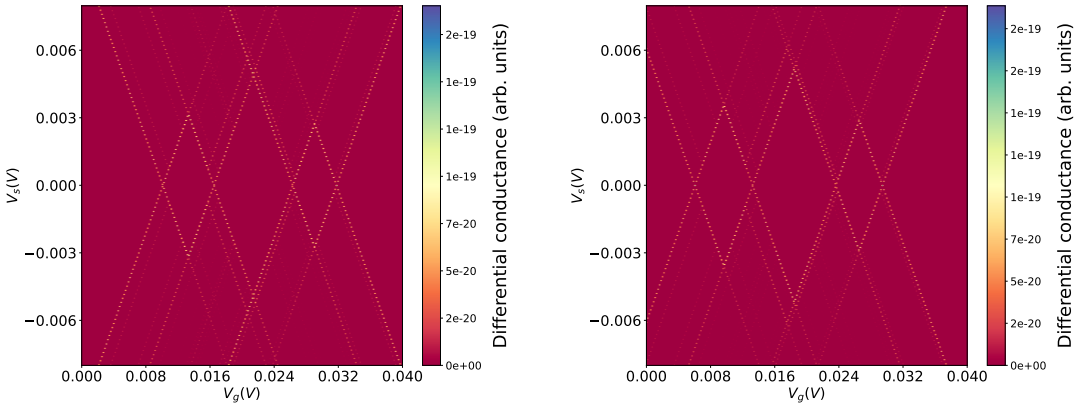

(a) SiGe Heterostructure Coulomb Diamonds with modified V_{BM}

(b) SiGe Heterostructure Coulomb Diamonds with GMSH modified structure

Figure 5.8. Coulomb Diamonds for the SiGe Heterostructure obtained in QTCAD [64]. On the left 5.8(a), Coulomb Diamonds with a modified V_{BM}, obtained in QTCAD [64]. On the right 5.8(b), Coulomb Diamonds with a GMSH modified structure, obtained in QTCAD [64].

5.2.3 Charge Stability Diagram

As discussed in Section 4.4, the Fermi-Hubbard Model offers a practical approach for simplifying the evaluation of Coulomb integrals in the context of double quantum dots. Specifically, the *get_coulomb_matrix* method within the many-body solver facilitates the computation of Coulomb interaction terms U_i and V_{ij} directly from

the Coulomb interaction matrix. Before conducting this computation, configuring the parameters of the many-body solver is essential. Notably, the number of states is set to four with a degeneracy of two. Furthermore, the Coulomb interaction matrix is computed without accounting for overlap terms. These terms typically emerge as atoms with unpaired electrons approach each other, resulting in a decrease in energy until a bond forms. In fact, after the bond formation, orbital energies reach a minimum. The energy released upon bond formation, derived from the difference between maximum and minimum orbital energies, is negligible compared to inter-dot and On-site Term Energy [66], thus justifying simplification.

Once the many-body solver is configured, computing the charge stability diagram becomes feasible. However, to speed-up computations, an approximation is proposed instead of adhering to the workflow employed for Coulomb Peaks and Coulomb Diamonds, using the sequential tunneling current (Equation 4.14). When the source-drain bias is sufficiently weak (in this case equal to zero), the dot system is at thermodynamic equilibrium with the leads. Therefore, the position of the transition lines in the charge stability diagram can be determined by computing the average particle addition spectrum, as described in Section 4.5.1.

In contrast with the approach of Coulomb Peaks and Coulomb Diamonds, the junction is not defined from the total device, but it is initialized from the many-body solver, which contains the single-particle energy levels, the Coulomb interaction matrix, and the lever arm matrix arrays (Section 4.3) that were previously calculated. Hence, the time calculation reduction occurs because the Coulomb interaction matrix is not computed again during the initialization of the junction, and the lever arm can be calculated for different bias configurations without solving the single-particle Schrödinger equation again. Additionally, the temperature is set to 10 K instead of 15 mK to obtain thicker transition lines in the addition spectrum. At this point, it is possible to compute the charge stability diagram by computing the addition spectrum for each configuration of the two plunger dot gate voltages. Specifically, the added voltages to the reference ones vary from 1 mV to 0.6 V.

From Figure 5.9(b) and Figure 5.9(a), two cases can be observed: one for low coupling between the dots (inter-dot barrier gate voltage equal to -0.35 V) and one for high coupling between the dots (inter-dot barrier gate voltage equal to -0.2 V). In the low coupling case, the two dots operate almost independently, where alterations in each gate voltage solely influence the corresponding dot's behavior. However, this is not the case of the high coupling scenario. If the two dots are capacitively coupled, an intriguing interplay emerges, where the voltage applied to one dot's gate directly impacts the behavior of the other dot through this capacitive interaction. Nevertheless, the presence of triple points in the transition of the low coupling charge stability diagram suggests a small interdependence between the dots in this scenario as well.

In conclusion, the interdependence underscores the complexity of quantum dot systems and highlights the importance of understanding their coupling mechanisms

for precise control and manipulation.

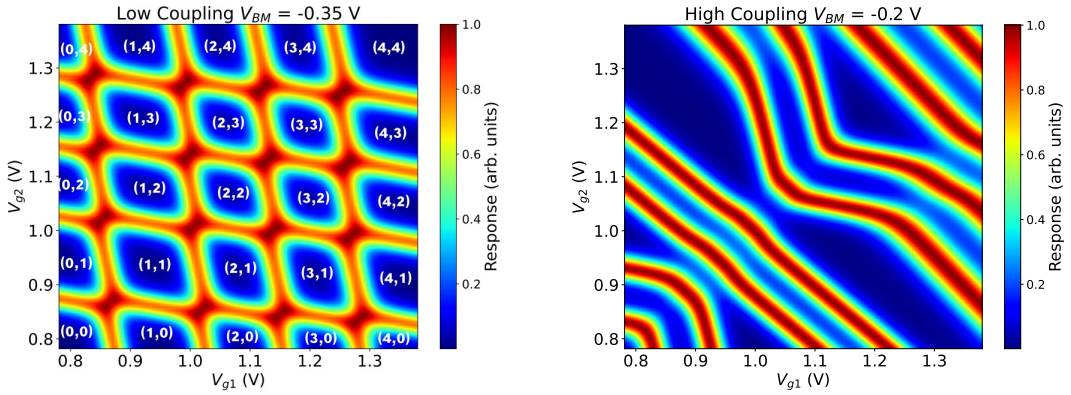

(a) SiGe heterostructure Charge Stability Diagram with V_{BM} equal to -0.35 V

(b) SiGe heterostructure Charge Stability Diagram with V_{BM} equal to -0.2 V

Figure 5.9. Charge Stability Diagrams for the SiGe heterostructure obtained in QTCAD [64]. On the left 5.9(a), the Charge Stability Diagrams for the SiGe heterostructure with V_{BM} equal to -0.35 V, resulting in low coupling between the dots, so they behave almost independently. On the right 5.9(b), the Charge Stability Diagrams for the SiGe heterostructure With V_{BM} equal to -0.2 V, resulting in high coupling between the dots, causes them to behave more like a single dot.

5.3 SiMOS Double Quantum Dot heterostructure Poisson-Schrödinger Analysis

Firstly, as done before, all simulation parameters are introduced. Specifically, the temperature is fixed at 15 mK and the dopant concentration is set to $N_D = 1 \times 10^{18}\,\mathrm{cm}^{-3}$, with complete ionization assumed. Additionally, the metal workfunction is:

$$\phi_m = \chi_{Si} + \frac{E_{g-Si}}{2} \tag{5.6}$$

where χ_{Si} is the electron affinity of Si and E_{g-Si} is the band gap energy of Si, respectively. Regarding the mesh obtained in GMSH, the node element size ranges from 8 nm in the bottom Si layer to 2 nm above and below the quantum layer, till 1 nm inside the quantum layer. Finally, it ranges from 8 nm to 2 nm inside the upper three gate layers. Furthermore, the applied voltages are introduced by

setting Dirichlet boundary conditions within the FEM solver:

$$\begin{aligned} V_{Y1} &= 535\,\text{mV} \\ V_{Y2} &= 535\,\text{mV} \\ V_{PL} &= 700\,\text{mV} \\ V_{PR} &= 700\,\text{mV} \\ V_{BL} &= 400\,\text{mV} \\ V_{BM} &= 40\,\text{mV} \\ V_{BR} &= 400\,\text{mV} \\ V_{RL} &= 1.3\,\text{V} \\ V_{RR} &= 1.3\,\text{V} \end{aligned} \tag{5.7}$$

where V_{Yi} is the applied voltage to the i-Y gate, V_{Pi} is the applied voltage to the i-Plunger gate, V_{Bi} is the applied voltage to the i-Barrier gate, and V_{Ri} is the applied voltage to the i-Reservoir gate. Here, R, L, and M respectively stand for right, left, and inter-dot. Moreover, considering what discussed in Section 4.6.2, an offset voltage of 199.06 µV is applied to the Right Dot Plunger, obtaining a symmetric potential profile.

5.3.1 Non-linear Poisson Equation

The first results of the simulation are obtained by solving the non-linear Poisson equation. In particular, as for the SiGe heterostructure, an iterative solution of the non-linear Poisson equation is performed, refining the mesh at each iteration until the error goes below a certain threshold set to 1×10^{-7}. Also in this case, the Conduction Band minimum is obtained by solving the non-linear Poisson. Analyzing Figure 5.10(a), the dark blue regions represent the four ohmic contacts (n+ doped area), while the light blue regions on the left and right represent the two reservoir gates. Furthermore, from the representation of the conduction band minimum, it is evident how well-defined the two quantum dots are inside the quantum layer. Similarly the previous case, the Poisson solution also provides insights into the classical electron population within the quantum layer, specifically at $z = 45$ nm, as depicted in Figure 5.10(b). In this representation, the quantum dots are not discernible, as a uniform distribution is observed, except for the four n+ doped regions (dark red) and the reservoir regions (light blue). This underscores the inadequacy of a classical analysis of carriers within the quantum layer, emphasising the necessity of employing a quantum mechanics approach.

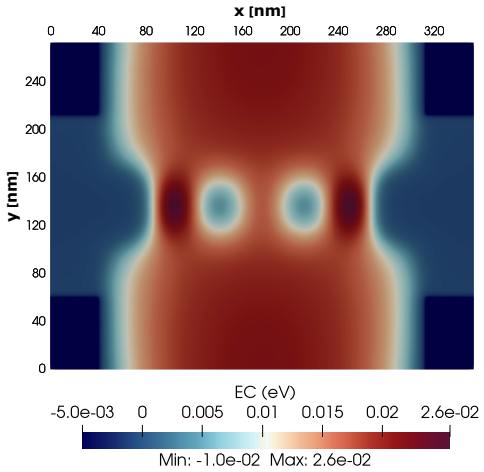

(a) SiMOS Double Quantum Dot heterostructure Conduction Band Minimum

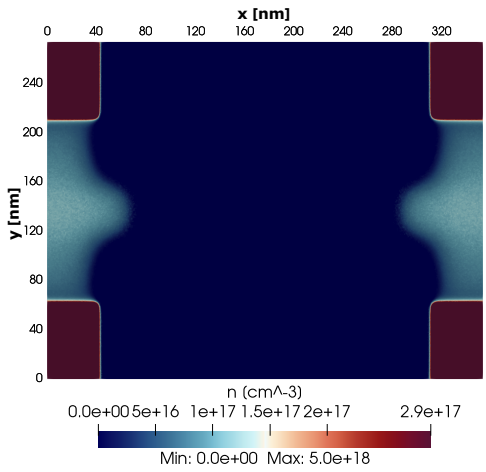

(b) SiMOS Double Quantum Dot heterostructure classical electrons density

Figure 5.10. Various properties of the SiMOS Double Quantum Dot heterostructure obtained by solving the Non-Linear Poisson Equation in QTCAD [64]. On the left 5.10(a), the SiMOS Double Quantum Dot heterostructure Conduction Band Minimum in the xy plane considering $z = 45$ nm, hence located inside the quantum layer, is obtained by solving the Non-Linear Poisson Equation in QTCAD [64]. On the right 5.10(b), the SiMOS Double Quantum Dot heterostructure classical electrons density in the xy plane considering $z = 45$ nm, hence located inside the quantum layer, is obtained by solving the Non-Linear Poisson Equation in QTCAD [64].

5.3.2 Single-Particle Schrödinger Equation

As in the previous SiGe heterostructure case, classical physics proves inadequate for analyzing the electron population within the quantum layer. Consequently, a quantum mechanics approach is adopted, involving the solution of the Single-Particle Schrödinger equation. Specifically, this equation is solved in the quantum region, which has the following dimensions:

- along the $\hat{x}$ axis, from $x = 96.5$ nm to 256.5 nm
- along the $\hat{y}$ axis, from $y = 60$ nm to 213 nm
- along the $\hat{z}$ axis, from $z = 35$ nm to 55 nm

In this case, the threshold error is set to 1×10^{-9}. Solving the Single-Particle Schrödinger Equation allows to determine the eigenstates and eigenenergies. Specifically, in Figure 5.11(a) and Figure 5.11(b), the cross-sections on the xy plane inside the quantum layer illustrate the bonding and antibonding eigenfunctions.

Notably, the wavefunction is equally distributed over the dots. Moreover, Figure 5.12 presents the eigenenergies of the first five eigenstates. Also in this case, as described in Section 4.3, it is obtained the lever arm matrix (Figure 5.13). Finally, considering the eigenenergies of Figure 5.12, it is computed an approximation of the tunneling coupling between the dots [65]:

$$t_0 \approx \frac{E_1 - E_0}{2} = 1.475 \text{ µeV} \implies 356.65 \text{ MHz} \tag{5.8}$$

where E_1 and E_0 are the first excited level energy and the ground state level energy respectively with zero detuning.

It also observes the behavior of the tunneling coefficient by modifying the inter-dot barrier voltage, keeping the other gate voltages fixed, as shown in Figure 5.14. In fact, for a high inter-dot barrier, the splitting of the levels decreases ($E_1 \approx E_0$) resulting in a low tunneling coefficient. Otherwise, a low inter-dot barrier means high splitting between E_1 and E_0, hence a high tunneling coefficient. As done for the eigenstate representation, the mesh asymmetries must be taken into account when the inter-dot barrier voltage is modified.

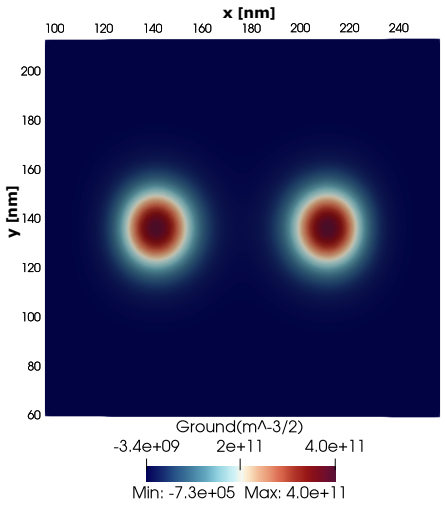

(a) Bonding single-particle eigenfunction in the xy plane

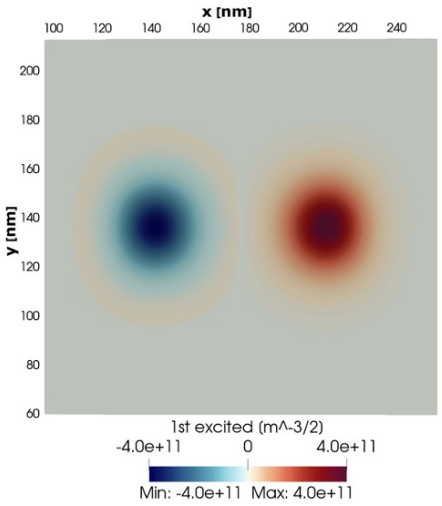

(b) Antibonding single-particle eigenfunction in the xy plane

Figure 5.11. Single-particle eigenfunction in the xy plane for the SiMOS Double Quantum Dot heterostructure. On the left 5.11(a), the Bonding single-particle eigenfunction located at $z = 45$ nm, hence inside the quantum layer. On the right 5.11(b), the Antibonding single-particle eigenfunction located at $z = 45$ nm, hence inside the quantum layer. Both are obtained by solving the Single-Particle Schrödinger Equation in QTCAD [64].

Energy Level	Energy [meV]
0	11.28923
1	11.29218
2	14.07295
3	14.08133
4	14.48267

Figure 5.12. Eigenenergies for the first five states of the SiMOS Double Quantum Dot heterostructure obtained by solving the Single-Particle Schrödinger Equation in QTCAD [64].

Energy Level	α_{PL}	α_{BM}	α_{PR}
0	1.275×10^{-1}	3.447×10^{-2}	1.275×10^{-1}
1	1.951×10^{-2}	3.439×10^{-2}	1.949×10^{-2}
2	1.066×10^{-1}	3.103×10^{-2}	1.791×10^{-2}
3	1.952×10^{-2}	3.085×10^{-2}	1.083×10^{-1}
4	1.015×10^{-1}	3.910×10^{-2}	1.011×10^{-1}

Figure 5.13. Lever Arm matrix of the SiMOS Double Quantum Dot heterostructure for the first five states, considering the two plungers gate and the inter–dot barrier gate of obtained by solving the Single-Particle Schrödinger Equation in QTCAD [64]. The voltage increment, to compute the Lever Arm matrix, is approximately equal to 5 mV

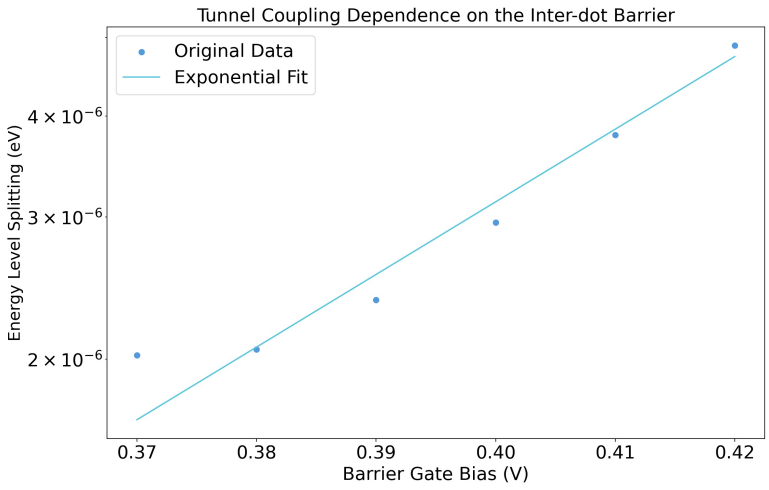

Figure 5.14. E_1 and E_0 splitting energy by changing the inter.dot barrier voltage for the SiMOS heterostructure obtained in QTCAD [64].

5.4 SiMOS Double Quantum Dot heterostructure Transport Analysis

As for the SiGe heterostructure, the transport analysis is fundamental for understanding how the electrons move between the quantum dot quantized energy levels, using this information to optimize the performance of qubits based on quantum dots. Also, it is performed a multi-particle Schrödinger description, as described in Section 4.4. Once the QTCAD Many-body solver is set up, it is possible to perform a transport analysis of our structure.

5.4.1 Coulomb Peaks

The Coulomb peaks are defined as done for the SiGe heterostructure. Furthermore, two solutions are explored: the first entails removing the inter-dot barrier by applying the same potential to the inter-dot barrier gate as that of the plunger gates, while the second involves modifying the structure in GMSH. This modification is depicted in Figure 5.15, where the inter-dot barrier gate is eliminated, leaving only a single large dot with a plunger gate.

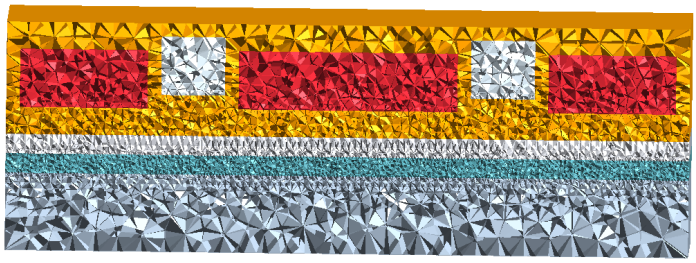

Figure 5.15. SiMOS modified Heterostructure obtained in GMSH [48], performing a cut along a plane perpendicular to the xy plane. Now, the structure has only one Dot Plunger in red, maintaining the other structure parameters are the same

Also in this case, the Coulomb peaks are computed for two states with degeneracy two, considering a drain-source voltage equal to 100 µV, a dot plunger gate

voltage interval from −0.01 to 0.05, the temperature is set to 1 K and the broadening of the energy level is set to 10 Hz by using a constant function to define it.

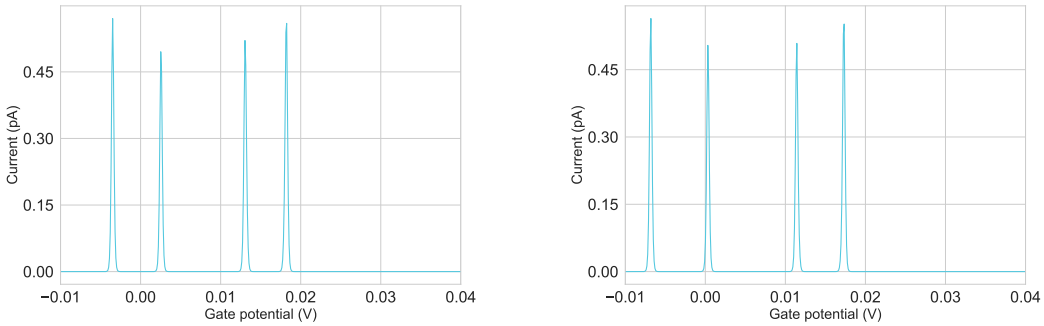

(a) Coulomb Peaks obtained in QTCAD [64], by applying the same potential of the two dot plungers to the inter-dot barrier.

(b) Coulomb Peaks obtained in QTCAD [64] by modifying the structure in GMSH

Figure 5.16. Coulomb Peaks for the SiMOS Heterostructure obtained in QTCAD [64]. On the left 5.16(a), Coulomb Peaks for the SiMOS Heterostructure with the same potential applied to the two dot plungers and the inter-dot barrier. On the right 5.16(b), Coulomb Peaks for the SiMOS Heterostructure with a modified structure in GMSH, reduced to one single big dot.

From Figure 5.16(a) and Figure 5.16(b), even though no magnetic field is applied during the simulation, for two states are observed four peaks with specific distances. Furthermore, the peaks heights, adopting the Equation 4.14, are due to the different values of the many-body transition rates for the various state obtained through Equation 4.15. All these aspects are the same already highlighted in Section 5.2.1. Both solutions yield similar results. However, small differences can be observed due to the variations in the potential profile obtained in the two solutions, Figure 5.17(a) and Figure 5.17(b). Unlike the SiGe case, it is not necessary to reduce the voltage applied to the plunger gate because the dot is not as deep as in the previous case.

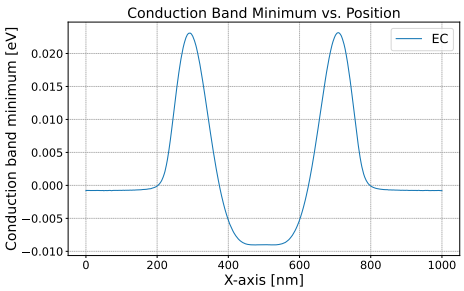

(a) SiMOS Heterostructure Conduction Band Minimum with modified V_{BM}

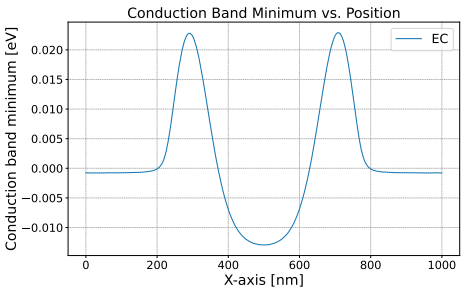

(b) SiMOS Heterostructure Conduction Band Minimum with GMSH modified structure

Figure 5.17. the Conduction Band Minimum for the SiMOS Heterostructure obtained in QTCAD [64]. On the left 5.17(a), the Conduction Band Minimum for the SiMOS Heterostructure with modified V_{BM}. On the right 5.17(b) the Conduction Band Minimum for the SiMOS Heterostructure with GMSH modified structure. Both images are cuts along the $\hat{x}$ axis at $y = 136.5$ nm and $z = 35$ nm.

5.4.2 Coulomb Diamonds

The Coulomb Diamonds describe the behavior of the differential conductance versus the source-drain voltage and the gate voltage, leveraging in QTCAD the same approximations as outlined in Section 5.2.2. Here, it is considered two states with a degeneracy of two for analysis. The source-drain voltage sweeps across a range of -8 mV to 8 mV, while the plunger dot gate voltage varies from -0.03 V to 0.05 V. Temperature is set to 1 K, and the broadening is fixed at 1 Hz, with a lever arm of the gate considered as one for simplicity. The resulting patterns of Coulomb diamonds, exemplified in Figure 5.8(a) and Figure 5.8(b), delineate regions of blockade where the count of electrons remains steady. As for the SiGe heterostructure scenario, the outcomes obtained through the two methods employed to reduce the structure to a single dot exhibit comparable results, with slight disparities due to variations in the potential profile. Furthermore, the analysis uncovers five distinct diamonds along the $\hat{x}$-axis, indicating five Coulomb blockade regions with a different electron. Notably, even without the presence of a magnetic field, five blockade regions are represented. The central diamond is larger compared to the two adjacent ones because it separates two different states, whereas the other two separate the same state with different numbers of electrons. In contrast to the SiGe Heterostructure situation, there is no necessity to reduce the voltage applied to the dot plunger, because the depth of the dot potential is not significant as for the SiGe case.

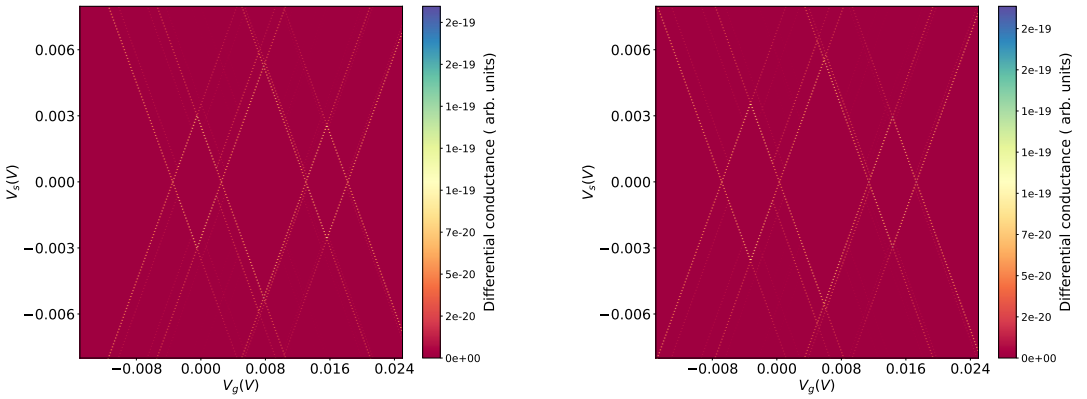

(a) SiMOS Heterostructure Coulomb Diamonds first solution

(b) SiMOS Heterostructure Coulomb Diamonds second solutions

Figure 5.18. Coulomb Diamonds for the SiMOS Heterostructure. On the left 5.18(a), the Coulomb Diamonds with a modified V_{BM}, obtained in QTCAD [64]. On the right 5.18(b), the Coulomb Diamonds with a GMSH modified structure, obtained in QTCAD [64].

5.4.3 Charge Stability Diagram

The approach used in Section 5.2.3 is replicated for the SiMOS heterostructure. Four states with degeneracy two are considered, and the overlap terms are omitted from the Coulomb interaction matrix, ensuring consistency with the SiGe Heterostructure case. Furthermore, the temperature is raised from 15 mK to 10 K to improve the visibility of transition lines in the charge stability diagram. Modifying the plunger gate voltages incrementally from the reference configuration by values ranging from 0.03 V to 0.5 V enables the computation of the charge stability diagram. For each bias configuration of the two plunger gate voltages, the addition particle spectrum is calculated. Figures 5.19(b) and 5.19(a) present two scenarios: one depicting low coupling between the dots (inter-dot barrier gate voltage equal to 0.25 V) and the other representing high coupling between the dots (inter-dot barrier gate voltage equal to 0.45 V). The results obtained for the SiMOS heterostructure mirror those of the SiGe heterostructure. In the case of low coupling, the two dots function almost independently, whereas in the high coupling scenario, this independence is reduced. In conclusion, the interdependence observed underscores the intricate nature of quantum dot systems.

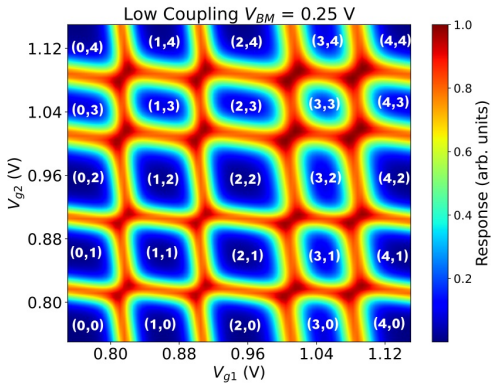

(a) SiMOS heterostructure Charge Stability Diagram with low coupling

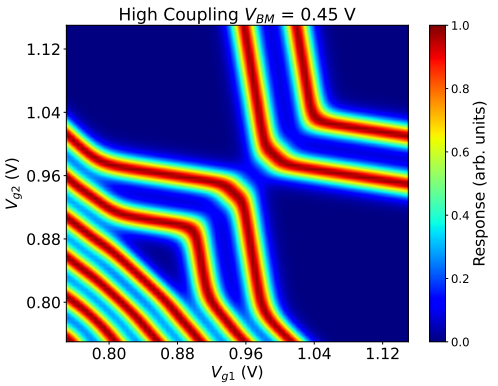

(b) SiMOS heterostructure Charge Stability Diagram with high coupling

Figure 5.19. Charge Stability Diagrams for the SiMOS heterostructure obtained using QTCAD [64]. On the left 5.19(a), The Charge Stability Diagram with V_{BM} equal to 0.25 V, showing low coupling between the dots thus they behave almost independently. On the right 5.19(b), The Charge Stability Diagram with V_{BM} equal to 0.45 V, showing high coupling between the dots where they behave more like a single dot.

Chapter 6

SiGe Four Quantum Dot Heterostructure Analysis

The goal of this chapter is to provide an extensive overview of the findings from modeling the SiGe heterostructure four-quantum-dot structure using QTCAD software. To be more precise, it replicates the methodology used in the analysis of the double-dot structures by only solving the Poisson and Schrödinger equations. Initially, all simulation parameters are introduced. The temperature is fixed at 15 mK, and the dopant concentration is set to $N_D = 1 \times 10^{18}\,\mathrm{cm}^{-3}$, with complete ionization assumed. Additionally, the metal workfunction is considered to be:

$$\phi_m = \chi_{Si_{0.7}Ge_{0.3}} + \frac{E_{g-Si_{0.7}Ge_{0.3}}}{2} \tag{6.1}$$

where $\chi_{Si_{0.7}Ge_{0.3}}$ and $E_{g-Si_{0.7}Ge_{0.3}}$ are the electron affinity and the band gap energy of $Si_{0.7}Ge_{0.3}$. Regarding the mesh, obtained in GMSH, the resolution of the mesh ranges from 4 nm in the bottom $Si_{0.7}Ge_{0.3}$ layer to 2 nm above and below the quantum layer, and 1 nm inside the quantum layer. Finally, it ranges from 4 to 2 nm inside the upper three gate layers. Moreover, the applied voltages are set

introducing Dirichlet Boundary conditions inside the FEM solver:

$$\begin{aligned} V_{Y1} &= 270mV \\ V_{Y2} &= 270mV \\ V_{PLU} &= 1.26V \\ V_{PRU} &= 1.26mV \\ V_{BLU} &= -530mV \\ V_{BMU} &= -810mV \\ V_{BRU} &= -520mV \\ V_{PLD} &= 1.26mV \\ V_{PRD} &= 1.26mV \\ V_{BLD} &= -520mV \\ V_{BMD} &= -810mV \\ V_{BRD} &= -530mV \\ V_{RL} &= 550mV \\ V_{RR} &= 550mV \end{aligned} \tag{6.2}$$

where V_{Yi} is the applied voltage to the i-Y gate, V_{Pil} is the applied voltage to the il-Plunger gate, V_{Bil} is the applied voltage to the il-Barrier gate, and V_{Ri} is the applied voltage to the i-Reservoir gate. R, L, and M respectively stand for right, left, and inter-dot while D and U stand for down and Up. Furthermore, considering what discussed in Section 4.6.2, an offset voltage of 9.65341 mV is applied to the Left Up Plunger, an offset voltage of 30.444 mV to the Right up Plunger and an offset voltage of 27.2793 mV to the Left down Plunger, obtaining a symmetric potential profile. V_{BRD} and V_{BLU} voltages are higher with respect to the V_{BRU} and V_{BLD} because the second two voltages are applied to the L barrier gates that have higher surfaces, as described in Section 3.3. Lastly, as discussed in Section 3.1, since QTCAD cannot simulate strain, a fictitious potential of -0.146 V is applied to the Si quantum layer. This adjustment aligns the minimum of the conduction band of $Si_{0.7}Ge_{0.3}$ with that of ^{28}Si

6.1 Non-linear Poisson Equation

An iterative solution of the non-linear Poisson equation is performed, refining the mesh at each iteration until the error goes below a certain threshold. The error threshold considered is again equal to 1×10^{-7} and specific refinement parameters

are set to achieve the convergence. Solving the Poisson equation allows the determination of the Conduction Band minimum, illustrated in Figure 6.1(a), where the dark blue areas denote the four ohmic contacts (n+ doped regions), and the light blue regions on the sides denote the two reservoir gates. Moreover, the representation of the conduction band minimum vividly demonstrates the well-defined nature of the four quantum dots within the quantum layer. Also in this case, from the Poisson solution the classical electron population within the quantum layer is obtained, specifically at $z = 34.5$ nm, as shown in Figure 6.1(b). In this representation, the quantum dots are not discernible, as a uniform distribution is observed, except for the four n+ doped regions (dark red) and the reservoir regions (light blue). This highlights the inadequacy of a classical analysis of carriers within the quantum layer, emphasizing the need of employing a quantum mechanics approach. Moreover, the behavior of the conduction band minimum along the y-axis for $z = 34.5$ nm and for different x values is outlined in Figure 6.2(b) and Figure 6.2(a). The images describe two different pairs of dots: one on the left part of the device and the other on the right. The height of the inter-dot barrier for both pairs is computed as the difference between the maximum of the inter-dot confinement potential and the minimum of the two dot valleys. In both figures, the barrier height is approximately 8 meV, indicating that the dots are well-defined and isolated.

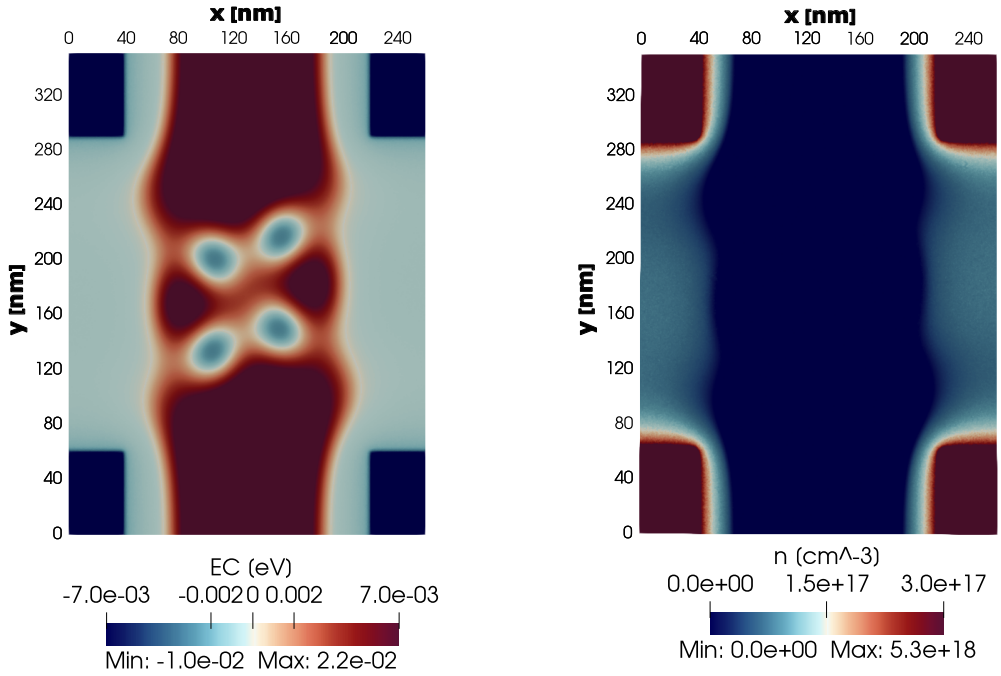

(a) SiGe Four Quantum Dot heterostructure Conduction Band Minimum

(b) SiGe Four Quantum Dot heterostructure classical electrons density

Figure 6.1. Various properties of the SiGe Four Quantum Dot heterostructure obtained by solving the Non-Linear Poisson Equation in QTCAD [64]. On the left 6.1(a), the SiGe Four Quantum Dot heterostructure Conduction Band Minimum in the xy plane considering $z = 34.5$ nm, hence located inside the quantum layer, is obtained by solving the Non-Linear Poisson Equation in QTCAD [64]. On the right 6.1(b), the SiGe Four Quantum Dot heterostructure classical electrons density in the xy plane considering $z = 34.5$ nm, hence located inside the quantum layer, is obtained by solving the Non-Linear Poisson Equation in QTCAD [64].

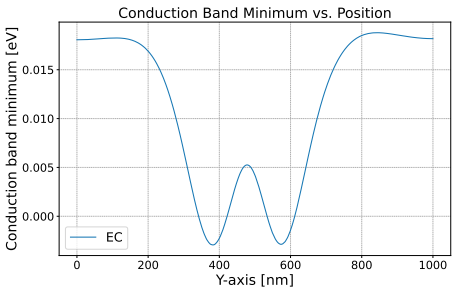

(a) The SiGe Four Quantum Dot heterostructure Conduction Band minimum of the two left dots

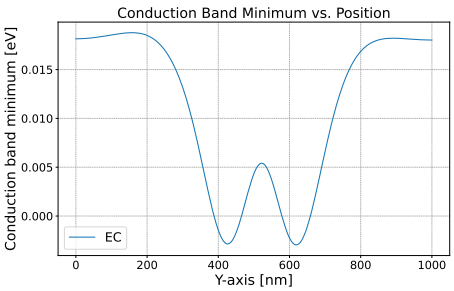

(b) The SiGe Four Quantum Dot heterostructure Conduction Band minimum of the two right dots

Figure 6.2. The SiGe Four Quantum Dot heterostructure Conduction Band minimum for different x position obtained by solving the Non-Linear Poisson Equation in QTCAD [64]. On the left 6.2(a),the SiGe Four Quantum Dot heterostructure Conduction Band Minimum along the y-axis at $z = 34.5$ nm, hence located inside the quantum layer, and $x = 105$ nm. On the right 6.2(b), the SiGe Four Quantum Dot heterostructure Conduction Band Minimum along the y-axis at $z = 34.5$ nm, hence located inside the quantum layer, and $x = 155$ nm

6.1.1 Single-Particle Schrödinger Equation

Classical physics is inadequate for analyzing the electron population within the quantum layer. Hence, a quantum mechanics approach is employed by solving the Single-Particle Schrödinger equation. Specifically, the Schrödinger equation is solved in the quantum region, which has the following dimensions:

- along the $\hat{x}$ axis, from $x = 70$ nm to 190 nm
- along the $\hat{y}$ axis, from $y = 60$ nm to 290 nm
- along the $\hat{z}$ axis, from $z = 25$ nm to 44 nm

In this case, the threshold error is set to 1×10^{-9}. From the solution of the Single-Particle Schrödinger Equation, the eigenstates and eigenenergies are obtained. In particular, Figure 6.3(a) and Figure 6.3(b), show the cuts on the xy plane inside the quantum layer, depicting the bonding and antibonding eigenfunctions. Moreover, to better describe the behavior of the wavefunction, the bonding, and antibonding states are also represented in the zy plane for different values of x, describing the different pairs of dots, as shown in Figure 6.4 and Figure 6.5. All these figures reveal an equal distribution of the wavefunction over the dots. Also in this case, Figure 6.6 lists the eigenenergies of the first five eigenstates.

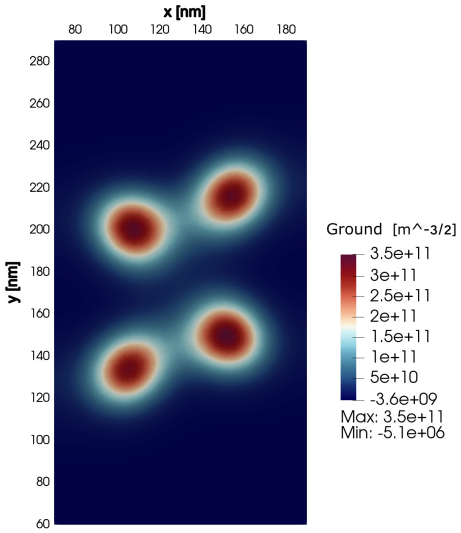

(a) Bonding single-particle eigenfunction in the xy plane

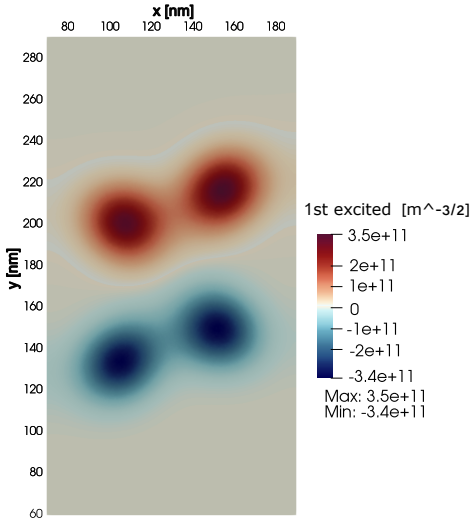

(b) Antibonding single-particle eigenfunction in the xy plane

Figure 6.3. Single-particle eigenfunction in the xy plane for the SiGe Four Quantum Dot heterostructure. On the left 6.3(a), the Bonding single-particle eigenfunction located at $z = 34.5$ nm, hence inside the quantum layer. On the right 6.3(b), the Antibonding single-particle eigenfunction located at $z = 34.5$ nm, hence inside the quantum layer. Both are obtained by solving the Single-Particle Schrödinger Equation in QTCAD [64].

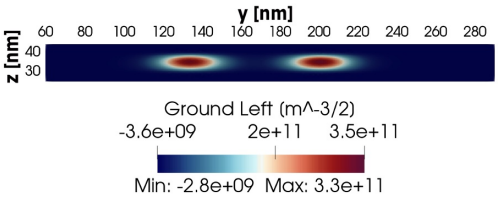

(a) Bonding Eigenstate left dots pair

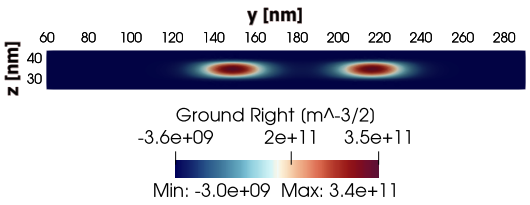

(b) Bonding Eigenstate right dots pair

Figure 6.4. In Figure 6.4(a) Bonding single-particle eigenfunction in the zy plane for the SiGe Four Quantum Dot heterostructure, located at $x = 105$ nm, is obtained by solving the Single-Particle Schrödinger Equation in QTCAD [64]. In Figure 6.4(b) Bonding single-particle eigenfunction in the zy plane for the SiGe Four Quantum Dot heterostructure, located at $x = 155$ nm, is obtained by solving the Single-Particle Schrödinger Equation in QTCAD [64].

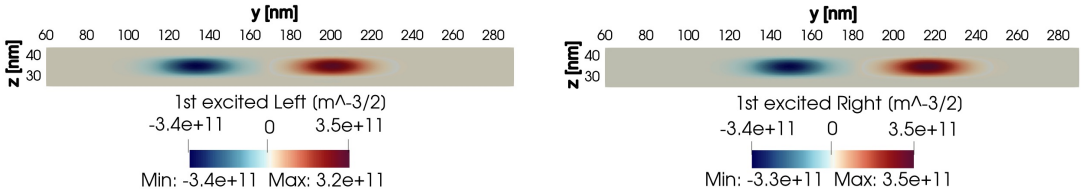

(a) Antibonding Eigenstate left dots pair (b) Antibonding Eigenstate right dots pair

Figure 6.5. In Figure 6.5(a) Antibonding single-particle eigenfunction in the zy plane for the SiGe Four Quantum Dot heterostructure, located at $x = 105$ nm, is obtained by solving the Single-Particle Schrödinger Equation in QTCAD [64]. In Figure 6.5(b), the Bonding single-particle eigenfunction in the zy plane for the SiGe Four Quantum Dot heterostructure located at $x = 155$ nm, is obtained by solving the Single-Particle Schrödinger Equation in QTCAD [64].

Energy Level	Energy [meV]
0	3.97546
1	3.98906
2	4.11922
3	4.11983
4	6.11319

Figure 6.6. Eigenenergies for the first five states of the SiGe Four Quantum Dot heterostructure obtained by solving the Single-Particle Schrödinger Equation in QTCAD [64].

The last result obtained through this analysis is the approximation of the tunneling coefficient between the two upper dots. As represented in Figure 6.7(a) and Figure 6.7(b), the two upper dots are isolated by applying a higher plunger voltage of 1.28 V and reducing the plunger voltage of the other two dots to 1.22 V. Additionally, an offset potential of 0.001634 V is applied to the left upper plunger gate to compensate for mesh asymmetries and achieve a wavefunction distributed across both dots. Ultimately, the tunneling coefficient is found to be:

$$t_0 \approx \frac{E_1 - E_0}{2} = 50 \text{ µeV} \implies 12.81 \text{ GHz} \tag{6.3}$$

The calculated value is much higher compared to the one obtained in the two double quantum dot cases. This is probably because the inter-dot barrier height between the dots is smaller than in previous cases, and the two dots are closer together in the four-dot heterostructure.

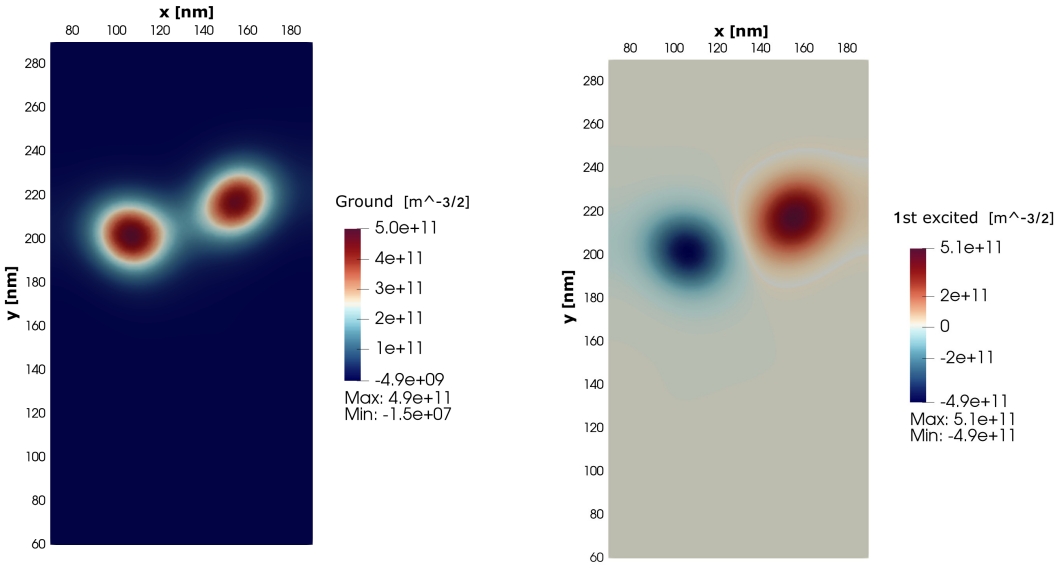

(a) The Bonding single-particle eigenfunction (b) The Antibonding single-particle eigenfunction

Figure 6.7. The single-particle eigenfunction in the xy plane for the SiGe Four Quantum Dot heterostructureOn the left 6.7(a), the Bonding single-particle eigenfunction located at $z = 34.5$ nm inside the quantum layer. On the right 6.7(b), the Antibonding single-particle eigenfunction located at $z = 34.5$ nm inside the quantum layer. Both are obtained by solving the Single-Particle Schrödinger Equation in QTCAD [64]. The images show wavefunctions distributed only over the two upper dots.

Chapter 7

Conclusions

The thesis aims to derive critical physical parameters from simulations of three heterostructures. The results obtained are fundamental for correctly implementing qubits within the analyzed devices.
The primary advantage lies in the ability to easily modify gate distances, gate dimensions, layer materials and dimensions, and to perform low-temperature simulations tasks typically complex in a physical laboratory.
Although QTCAD may not entirely match the accuracy of real-world experiments, it provides valuable insights into device behavior. The goal is to perform these simulations to evaluate the device's feasibility for real-world applications and efficiently assess its response to structural parameter modifications. Consequently, structural changes can be made by simply altering the simulation code, avoiding the need for repetitive and expensive lithographic processes.
The transport analysis of the double quantum dot structures demonstrates the single-electron regime, which is fundamental for precise control and manipulation of qubits implemented through the double quantum dot heterostructure. Furthermore, the charge stability diagram in low coupling cases shows that the two dots exhibit a small interdependence, even when well defined and isolated. This aspect must be considered for the correct implementation of quantum logic gates through this heterostructure.
In the case of four quantum dots, it is interesting to observe the formation of well-defined and isolated dots even when the dimensions of the gates and the distances between them are smaller compared to the two quantum dots cases. Moreover, in the four quantum dots configuration, the tunneling coefficient approximation between the two upper dots is much higher compared to the other configurations. The higher tunneling coefficient between the two upper dots in the four quantum dots configuration is likely due to their smaller inter-dot barrier and closer proximity. These results suggest potential applications in implementing two and four quantum logic gates using such heterostructures.
An interesting future perspective is to extend the Fermi-Hubbard model, described

in [50], to define four qubits and simulate more complex logic gates with the four quantum dots structure. Additionally, performing a transport analysis of the four quantum dots heterostructure could provide insights into the interdependence among the dots, crucial for manipulating qubits created through this device. Another possibility is to explore hole spin qubits with Germanium quantum dots in QTCAD presents another intriguing avenue. However, solving the Schrödinger equation for holes is more complex, as their physics is predominantly influenced by the valence band maximum, which is degenerate or nearly degenerate at the Γ point in semiconductors with a diamond lattice. In QTCAD, the four-band Luttinger-Kohn model is utilized to describe materials with a diamond crystal structure, focusing on the two-fold-degenerate valence bands: heavy-hole and light-hole bands, while neglecting the split-off valence bands [67]. Finally, it is possible to exploit the $\hat{z}$ direction to increase the amount of qubits. This can be accomplished by adding another Si quantum layer to the heterostructure and including a back gate to control the quantum dots in the two quantum layers independently. Although QTCAD idealizes many aspects, the obtained results serve as a valuable starting point for understanding device behavior before experimental realization in the lab.

Bibliography

[1] Thomas Ihn. *Semiconductor Nanostructures: Quantum states and electronic transport*. OUP Oxford, 2009.

[2] Hendrik Bluhm, Thomas Brückel, Markus Morgenstern, Gero Plessen, and Christoph Stampfer. *Electrons in Solids: Mesoscopics, Photonics, Quantum Computing, Correlations, Topology*. Walter de Gruyter GmbH & Co KG, 2019.

[3] Guido Burkard, Thaddeus D. Ladd, Andrew Pan, John M. Nichol, and Jason R. Petta. Semiconductor spin qubits. *Rev. Mod. Phys.*, 95:025003, Jun 2023.

[4] Line Hjortshøj Pedersen, Niels Martin Møller, and Klaus Mølmer. Fidelity of quantum operations. *Physics Letters A*, 367(1-2):47–51, 2007.

[5] Floris A. Zwanenburg, Andrew S. Dzurak, Andrea Morello, Michelle Y. Simmons, Lloyd C. L. Hollenberg, Gerhard Klimeck, Sven Rogge, Susan N. Coppersmith, and Mark A. Eriksson. Silicon quantum electronics. *Rev. Mod. Phys.*, 85:961–1019, Jul 2013.

[6] NS Lai, WH Lim, CH Yang, FA Zwanenburg, WA Coish, F Qassemi, A Morello, and AS Dzurak. Pauli spin blockade in a highly tunable silicon double quantum dot. *Scientific reports*, 1(1):110, 2011.

[7] Hiroki Noda, Shumpei Sakaguchi, Ryoga Fujita, Susumu Minami, Hiroyuki Hirakata, and Takahiro Shimada. Electronic strengthening mechanism of covalent si via excess electron/hole doping. *Scientific Reports*, 13(1):16546, 2023.

[8] Nicolas Large. Resonant raman-brillouin scattering in semiconductor and metallic nanostructures: from nano-acoustics to acousto-plasmonics. 10 2011.

[9] Eric G Barbagiovanni, David J Lockwood, Peter J Simpson, and Lyudmila V Goncharova. Quantum confinement in si and ge nanostructures: Theory and experiment. *Applied Physics Reviews*, 1(1), 2014.

[10] Mohammed Abdelmajeed Mohammed Ibrahim Darwish. *Quantum Dots Chalcogenides Based Solar Cells; Synthesis and Characterization.* PhD thesis, Alexandria University, 2015.

[11] F Simmel, David Abusch-Magder, DA Wharam, MA Kastner, and JP Kotthaus. Statistics of the coulomb-blockade peak spacings of a silicon quantum dot. *Physical Review B*, 59(16):R10441, 1999.

[12] JM Elzerman, R Hanson, LH Willems van Beveren, Seigo Tarucha, LMK Vandersypen, and LP Kouwenhoven. Semiconductor few-electron quantum dots as spin qubits. *Quantum dots: A doorway to nanoscale physics*, pages 25–95, 2005.

[13] Tetsuo Kodera, Thierry Ferrus, Toshihiro Nakaoka, Gareth Podd, Michael Tanner, David Williams, and Yasuhiko Arakawa. Fine and large coulomb diamonds in a silicon quantum dot. *Japanese Journal of Applied Physics*, 48(6S):06FF15, 2009.

[14] S Bednarek, B Szafran, and JJPRB Adamowski. Theoretical description of electronic properties of vertical gated quantum dots. *Physical Review B*, 64(19):195303, 2001.

[15] J Adamowski, S Bednarek, and B Szafran. Configuration interaction study of the single-electron transport in the vertical gated quantum dot. *physica status solidi (b)*, 237(1):289–295, 2003.

[16] Ronald Hanson, Leo P Kouwenhoven, Jason R Petta, Seigo Tarucha, and Lieven MK Vandersypen. Spins in few-electron quantum dots. *Reviews of modern physics*, 79(4):1217, 2007.

[17] Wilfred G Van der Wiel, Silvano De Franceschi, Jeroen M Elzerman, Toshimasa Fujisawa, Seigo Tarucha, and Leo P Kouwenhoven. Electron transport through double quantum dots. *Reviews of modern physics*, 75(1):1, 2002.

[18] Lieven M. K. Vandersypen and Mark A. Eriksson. Quantum computing with semiconductor spins. *Physics Today*, 72(8):38–45, 08 2019.

[19] MA Eriksson, SN Coppersmith, and MG Lagally. Semiconductor quantum dot qubits. *MRS bulletin*, 38(10):794–801, 2013.

[20] Andrea Morello, Jarryd J. Pla, Floris A. Zwanenburg, Kok W. Chan, Kuan Y. Tan, Hans Huebl, Mikko Möttönen, Christopher D. Nugroho, Changyi Yang, Jessica A. van Donkelaar, Andrew D. C. Alves, David N. Jamieson, Christopher C. Escott, Lloyd C. L. Hollenberg, Robert G. Clark, and Andrew S. Dzurak. Single-shot readout of an electron spin in silicon. *Nature*, 467(7316):687–691, September 2010.

[21] J. R. Weber, W. F. Koehl, J. B. Varley, A. Janotti, B. B. Buckley, C. G. Van de Walle, and D. D. Awschalom. Quantum computing with defects. *Proceedings of the National Academy of Sciences*, 107(19):8513–8518, 2010.

[22] Anasua Chatterjee, Paul Stevenson, Silvano De Franceschi, Andrea Morello, Nathalie P de Leon, and Ferdinand Kuemmeth. Semiconductor qubits in practice. *Nature Reviews Physics*, 3(3):157–177, 2021.

[23] Tsuneya Ando, Alan B Fowler, and Frank Stern. Electronic properties of two-dimensional systems. *Reviews of Modern Physics*, 54(2):437, 1982.

[24] Daniel Loss and David P. DiVincenzo. Quantum computation with quantum dots. *Phys. Rev. A*, 57:120–126, Jan 1998.

[25] J Gorman, DG Hasko, and DA Williams. Charge-qubit operation of an isolated double quantum dot. *Physical review letters*, 95(9):090502, 2005.

[26] Xin Zhang, Hai-Ou Li, Gang Cao, Ming Xiao, Guang-Can Guo, and Guo-Ping Guo. Semiconductor quantum computation. *National Science Review*, 6(1):32–54, 12 2018.

[27] Xian Wu, D. R. Ward, J. R. Prance, Dohun Kim, John King Gamble, R. T. Mohr, Zhan Shi, D. E. Savage, M. G. Lagally, Mark Friesen, S. N. Coppersmith, and M. A. Eriksson. Two-axis control of a singlet–triplet qubit with an integrated micromagnet. *Proceedings of the National Academy of Sciences*, 111(33):11938–11942, 2014.

[28] Qiuzi Li, Łukasz Cywiński, Dimitrie Culcer, Xuedong Hu, and S Das Sarma. Exchange coupling in silicon quantum dots: Theoretical considerations for quantum computation. *Physical Review B*, 81(8):085313, 2010.

[29] Fabio Baruffa, Peter Stano, and Jaroslav Fabian. Spin-orbit coupling and anisotropic exchange in two-electron double quantum dots. *Physical Review B*, 82(4):045311, 2010.

[30] OE Dial, Michael Dean Shulman, Shannon Pasca Harvey, H Bluhm, V Umansky, and Amnon Yacoby. Charge noise spectroscopy using coherent exchange oscillations in a singlet-triplet qubit. *Physical review letters*, 110(14):146804, 2013.

[31] Clement H Wong, MA Eriksson, SN Coppersmith, and Mark Friesen. High-fidelity singlet-triplet s- t- qubits in inhomogeneous magnetic fields. *Physical Review B*, 92(4):045403, 2015.

[32] Jacob Z Blumoff, Andrew S Pan, Tyler E Keating, Reed W Andrews, David W Barnes, Teresa L Brecht, Edward T Croke, Larken E Euliss, Jacob A Fast,

Clayton AC Jackson, et al. Fast and high-fidelity state preparation and measurement in triple-quantum-dot spin qubits. *PRX Quantum*, 3(1):010352, 2022.

[33] David P DiVincenzo, Dave Bacon, Julia Kempe, Guido Burkard, and K Birgitta Whaley. Universal quantum computation with the exchange interaction. *nature*, 408(6810):339–342, 2000.

[34] J Medford, Johannes Beil, JM Taylor, EI Rashba, H Lu, AC Gossard, and Charles M Marcus. Quantum-dot-based resonant exchange qubit. *Physical review letters*, 111(5):050501, 2013.

[35] Zhan Shi, CB Simmons, JR Prance, John King Gamble, Teck Seng Koh, Yun-Pil Shim, Xuedong Hu, DE Savage, MG Lagally, MA Eriksson, et al. Fast hybrid silicon double-quantum-dot qubit. *Physical review letters*, 108(14):140503, 2012.

[36] Dohun Kim, Zhan Shi, CB Simmons, DR Ward, JR Prance, Teck Seng Koh, John King Gamble, DE Savage, MG Lagally, Mark Friesen, et al. Quantum control and process tomography of a semiconductor quantum dot hybrid qubit. *Nature*, 511(7507):70–74, 2014.

[37] Srijit Goswami, KA Slinker, Mark Friesen, LM McGuire, JL Truitt, Charles Tahan, LJ Klein, JO Chu, PM Mooney, Daniel W Van Der Weide, et al. Controllable valley splitting in silicon quantum devices. *Nature Physics*, 3(1):41–45, 2007.

[38] Frank Stern and WE Howard. Properties of semiconductor surface inversion layers in the electric quantum limit. *Physical Review*, 163(3):816, 1967.

[39] FF Fang and WE Howard. Negative field-effect mobility on (100) si surfaces. *Physical Review Letters*, 16(18):797, 1966.

[40] Xinyu Zhao and Xuedong Hu. Measurement of tunnel coupling in a si double quantum dot based on charge sensing. *Physical Review Applied*, 17(6):064043, 2022.

[41] John King Gamble, Patrick Harvey-Collard, N Tobias Jacobson, Andrew D Baczewski, Erik Nielsen, Leon Maurer, Inès Montaño, Martin Rudolph, MS Carroll, CH Yang, et al. Valley splitting of single-electron si mos quantum dots. *Applied Physics Letters*, 109(25), 2016.

[42] Matthew G Borselli, Richard S Ross, Andrey A Kiselev, Edward T Croke, Kevin S Holabird, Peter W Deelman, Leslie D Warren, Ivan Alvarado-Rodriguez, Ivan Milosavljevic, Fiona C Ku, et al. Measurement of valley splitting in high-symmetry si/sige quantum dots. *Applied Physics Letters*, 98(12), 2011.

[43] Mark Friesen, Sucismita Chutia, Charles Tahan, and SN Coppersmith. Valley splitting theory of si ge/ si/ si ge quantum wells. *Physical Review B*, 75(11):115318, 2007.

[44] Gang Wang, Zhi-Gang Song, Jun-Wei Luo, and Shu-Shen Li. Origin of giant valley splitting in silicon quantum wells induced by superlattice barriers. *Physical Review B*, 105(16):165308, 2022.

[45] AJ Sigillito, JC Loy, DM Zajac, MJ Gullans, LF Edge, and JR Petta. Site-selective quantum control in an isotopically enriched si 28/si 0.7 ge 0.3 quadruple quantum dot. *Physical Review Applied*, 11(6):061006, 2019.

[46] M Steger, K Saeedi, MLW Thewalt, JJL Morton, H Riemann, NV Abrosimov, P Becker, and H-J Pohl. Quantum information storage for over 180 s using donor spins in a 28si "semiconductor vacuum". *Science*, 336(6086):1280–1283, 2012.

[47] Lucy VC Assali, Helena M Petrilli, Rodrigo B Capaz, Belita Koiller, Xuedong Hu, and S Das Sarma. Hyperfine interactions in silicon quantum dots. *Physical Review B*, 83(16):165301, 2011.

[48] Christophe Geuzaine and Jean-François Remacle. Gmsh: A 3-d finite element mesh generator with built-in pre-and post-processing facilities. *International journal for numerical methods in engineering*, 79(11):1309–1331, 2009.

[49] WIL Lawrie, HGJ Eenink, NW Hendrickx, JM Boter, L Petit, SV Amitonov, M Lodari, B Paquelet Wuetz, C Volk, SGJ Philips, et al. Quantum dot arrays in silicon and germanium. *Applied Physics Letters*, 116(8), 2020.

[50] Davide Costa, Mario Simoni, Gianluca Piccinini, and Mariagrazia Graziano. Advances in modelling of noisy quantum computers: Spin qubits in semiconductor quantum dots. *IEEE Access*, 2023.

[51] Florian K Unseld, Marcel Meyer, Mateusz T Mądzik, Francesco Borsoi, Sander L de Snoo, Sergey V Amitonov, Amir Sammak, Giordano Scappucci, Menno Veldhorst, and Lieven MK Vandersypen. A 2d quantum dot array in planar 28si/sige. *Applied Physics Letters*, 123(8), 2023.

[52] Ioanna Kriekouki, Félix Beaudoin, Pericles Philippopoulos, Chenyi Zhou, Julien Camirand Lemyre, Sophie Rochette, Salvador Mir, Manuel J Barragan, Michel Pioro-Ladrière, and Philippe Galy. Interpretation of 28 nm fd-soi quantum dot transport data taken at 1.4 k using 3d quantum tcad simulations. *Solid-State Electronics*, 194:108355, 2022.

[53] Ioanna Kriekouki, Pericles Philippopoulos, Félix Beaudoin, Salvador Mir, Manuel J Barragan, Michel Pioro-Ladrière, and Philippe Galy. Simulation

process flow for the implementation of industry-standard fd-soi quantum dot devices. *Solid-State Electronics*, 209:108777, 2023.

[54] R Winkler, S Papadakis, E De Poortere, and M Shayegan. *Spin-orbit coupling in two-dimensional electron and hole systems*, volume 41. Springer, 2003.

[55] Yasuhiro Tokura, Wilfred G van der Wiel, Toshiaki Obata, and Seigo Tarucha. Coherent single electron spin control in a slanting zeeman field. *Physical review letters*, 96(4):047202, 2006.

[56] Witold Trzeciakowski. Effective-mass approximation in semiconductor heterostructures: One-dimensional analysis. *Physical Review B*, 38(17):12493, 1988.

[57] Andreas Fuhrer. *Phase coherence, orbital and spin states in quantum rings.* PhD thesis, ETH Zurich, 2003.

[58] FA Mohiyaddin, G Simion, NI Dumoulin Stuyck, R Li, A Elsayed, M Shehata, S Kubicek, C Godfrin, BT Chan, J Jussot, et al. Tcad-assisted multiphysics modeling & simulation for accelerating silicon quantum dot qubit design. In *2020 International Conference on Simulation of Semiconductor Processes and Devices (SISPAD)*, pages 253–256. IEEE, 2020.

[59] AD Güçlü, Qing Feng Sun, Hong Guo, and R Harris. Geometric blockade in a quantum dot: Transport properties by exact diagonalization. *Physical Review B*, 66(19):195327, 2002.

[60] S Bednarek, B Szafran, and J Adamowski. Solution of the poisson-schrödinger problem for a single-electron transistor. *Physical Review B*, 61(7):4461, 2000.

[61] Henrik Bruus and Karsten Flensberg. *Many-body quantum theory in condensed matter physics: an introduction.* OUP Oxford, 2004.

[62] Toivo Hensgens, Takafumi Fujita, Laurens Janssen, Xiao Li, CJ Van Diepen, Christian Reichl, Werner Wegscheider, Sankar Das Sarma, and Lieven MK Vandersypen. Quantum simulation of a fermi–hubbard model using a semiconductor quantum dot array. *Nature*, 548(7665):70–73, 2017.

[63] DG Deppe and H Huang. Fermi's golden rule, nonequilibrium electron capture from the wetting layer, and the modulation response in p-doped quantum-dot lasers. *IEEE journal of quantum electronics*, 42(3):324–330, 2006.

[64] Félix Beaudoin, Pericles Philippopoulos, Chenyi Zhou, Ioanna Kriekouki, Michel Pioro-Ladrière, Hong Guo, and Philippe Galy. Robust technology computer-aided design of gated quantum dots at cryogenic temperature. *Applied physics letters*, 120(26), 2022.

[65] L-X Zhang, DV Melnikov, and J-P Leburton. Non-monotonic variation of the exchange energy in double elliptic quantum dots. In *Physical Models for Quantum Dots*, pages 321–336. Jenny Stanford Publishing, 2021.

[66] Bilal Tariq and Xuedong Hu. Impact of the valley orbit coupling on exchange gate for spin qubits in silicon quantum dots. *arXiv preprint arXiv:2107.00732*, 2021.

[67] Thomas B. Bahder. Eight-band k·p model of strained zinc-blende crystals. *Phys. Rev. B*, 41:11992–12001, Jun 1990.